Intratumoral *Fusobacterium nucleatum* Recruits Tumor-Associated Neutrophils to Promote Gastric Cancer Progression and Immune Evasion

Tianhao Zhang[1,2,3], Ying Li[4], Ertao Zhai[1,2], Risheng Zhao[1,2], Yan Qian[1,2], Zhixin Huang[1,2,3], Yinan Liu[1,2,3], Zeyu Zhao[1,2,3], Xiang Xu[1,2,3], Jianqiu Liu[1,2,3], Zikang Li[1,2,3], Zhi Liang[1,2,3], Ran Wei[1,2,3], Linying Ye[1,2,3], Jinping Ma[1,2], Qingping Wu[4], Jianhui Chen[1,2,5], and Shirong Cai[1,2]

ABSTRACT

Intratumoral microbiota can affect the development and progression of many types of cancer, including gastric cancer. A better understanding of the precise mechanisms by which microbiota support gastric cancer could lead to improved therapeutic approaches. In this study, we investigated the effect of intratumoral microbiota on the tumor immune microenvironment during gastric cancer malignant progression. Analysis of human gastric cancer tissues with 16S rRNA amplicon sequencing revealed that *Fusobacterium nucleatum* was significantly enriched in gastric cancer tissues with lymph node metastasis and correlated with a poor prognosis. *F. nucleatum* infection spontaneously induced chronic gastritis and promoted gastric mucosa dysplasia in mice. Furthermore, gastric cancer cells infected with *F. nucleatum* showed accelerated growth in immunocompetent mice compared with immunodeficient mice. Single-cell RNA sequencing uncovered that *F. nucleatum* recruited tumor-associated neutrophils (TAN) to reshape the tumor immune microenvironment. Mechanistically, *F. nucleatum* invaded gastric cancer cells and activated IL17/NF-κB/RelB signaling, inducing TAN recruitment. *F. nucleatum* also stimulated TAN differentiation into the protumoral subtype and subsequent promotion of PD-L1 expression, further facilitating gastric cancer immune evasion while also enhancing the efficacy of anti–PD-L1 antibody therapy. Together, these data uncover mechanisms by which *F. nucleatum* affects gastric cancer immune evasion and immunotherapy efficacy, providing insights for developing effective treatment strategies.

Significance: Intratumoral *F. nucleatum* activates NF-κB signaling to facilitate gastric cancer immune evasion by promoting tumor-associated neutrophil recruitment that sensitizes tumors to immune checkpoint blockade therapy.

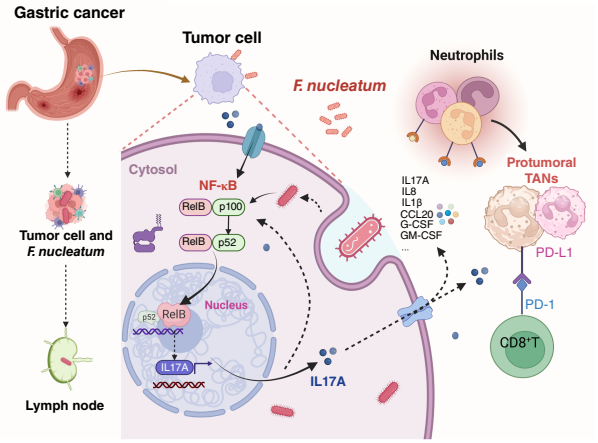

Introduction

Gastric cancer is the fifth most prevalent cancer worldwide, accounting for approximately 5.6% of all cancer cases. It is the fourth leading cause of cancer death, accounting for 7.7% of such mortalities (1). However, strategies for early diagnosis and treatment of gastric cancer are still inadequate. Emerging research indicates that apart from *Helicobacter pylori*, other microbial communities may contribute to the progression of gastric cancer

[1]Division of Gastrointestinal Surgery Center, the First Affiliated Hospital, Sun Yat-sen University, Guangzhou, China. [2]Gastric Cancer Center, Sun Yat-sen University, Guangzhou, Guangdong, China. [3]Laboratory of General Surgery, the First Affiliated Hospital, Sun Yat-sen University, Guangzhou, Guangdong, China. [4]Guangdong Provincial Key Laboratory of Microbial Safety and Health, National Health Commission Science and Technology Innovation Platform for Nutrition and Safety of Microbial Food, State Key Laboratory of Applied Microbiology Southern China, Institute of Microbiology, Guangdong Academy of Sciences, Guangzhou, China. [5]Department of General Surgery, Guangxi Hospital Division of The First Affiliated Hospital, Sun Yat-sen University, Nanning, Guangxi, China.

T. Zhang, Y. Li, and E. Zhai contributed equally to this article.

Corresponding Authors: Qingping Wu, Guangdong Provincial Key Laboratory of Microbial Safety and Health, National Health Commission Science and Technology Innovation Platform for NAutrition and Safety of Microbial Food, State Key Laboratory of Applied Microbiology Southern China, Institute of Microbiology, Guangdong Academy of Sciences, No. 100 Xianlie Middle Road, Yuexiu District, Guangzhou, 510070, Guangdong, China. E-mail: wuqp203@163.com; Jianhui Chen, Division of Gastrointestinal Surgery Center, the First Affiliated Hospital, Sun Yat-sen University, No. 58 Zhongshan Second Road, Yuexiu District, Guangzhou, 510080, Guangdong, China; Department of General Surgery, Guangxi Hospital Division of The First Affiliated Hospital, Sun Yat-sen University, No. 3 Foziling Road, Qingxiu District, Nanning 530028, Guagnxi, China. E-mail: chenjh45@mail.sysu.edu.cn; and Shirong Cai, Division of Gastrointestinal Surgery Center, the First Affiliated Hospital, Sun Yat-sen University, No. 58 Zhongshan Second Road, Yuexiu District, Guangzhou, 510080, Guangdong, China. E-mail: caishr@mail.sysu.edu.cn

Cancer Res 2025;85:1819–41

doi: 10.1158/0008-5472.CAN-24-2580

(2–4). Yu and colleagues (5) identified a novel pathogenic bacterium for gastric cancer, *Streptococcus anginosus*, which interacts directly with gastric mucosal epithelial cells and fosters gastric cancer development by modulating the TMPC-ANXA2-MAPK axis. Nevertheless, the precise mechanisms by which intratumoral microbiota affect gastric cancer's malignant progression and tumor immune microenvironment (TIME) remain elusive.

Recent studies have been increasingly focusing on exploring the impact of intratumoral microbiota on malignant tumor progression and TIME. The significance of tumor-associated neutrophils (TAN) in tumor advancement has gained notable attention recently, chiefly because of their distinctive subtypes and influence on neoplastic growth. The two main subtypes of neutrophils, N1 and N2, encompass antitumor and protumor properties, respectively (6–8). Recent research has underscored the significant role of TANs in regulating the TIME and antitumor immune responses (9, 10). Nevertheless, the interplay between the microbiota and TANs in gastric cancer and how TANs can influence the TIME, leading to alterations in malignant progression, remains poorly elucidated. Moreover, their impact on modulating immune checkpoint inhibitor efficacy is frequently undervalued in current literature.

This study primarily aimed to examine the potential influence of intratumoral microbiota on the progression of gastric cancer and its interaction with the TIME. In this study, *F. nucleatum* was identified as a novel non–*H. pylori* pathogen that promotes gastric cancer immune evasion and boosts immunotherapy efficacy. This gram-negative, nonspore-forming opportunistic commensal anaerobe is predominantly found in the oral cavity and has been linked to various manifestations in periodontal diseases and cancer (11–15). Recent research has shed light on the role of *F. nucleatum* in the development of gastrointestinal cancers (16). Particularly, *F. nucleatum* promotes tumorigenesis (12), inhibits cancer cell apoptosis (13), and induces resistance to chemotherapy (17). However, the precise involvement of *F. nucleatum* in gastric cancer malignant progression and its specific pathogenic molecular mechanisms remain largely ambiguous. In the current study, *F. nucleatum* was found to invade gastric cancer cells and activate IL17 signaling, which in turn promotes the recruitment of neutrophils and the differentiation of PD-L1$^+$ TANs. This contributes to the exhaustion of CD8$^+$ T cells, facilitating immune evasion in gastric cancer and augmenting the effectiveness of PD-L1 immune therapy. Our study has identified a novel non–*H. pylori* pathogen, *F. nucleatum*, which plays a crucial role in immune evasion in gastric cancer and modulates the response to immunotherapy.

Materials and Methods

Patient and tissue specimens

Tumor tissues were collected from 133 patients [40 patients between 2020 and 2022 (cohort 1) and 93 patients between 2004 and 2007 (cohort 2)] with gastric cancer treated at the First Affiliated Hospital of Sun Yat-sen University (Guangzhou, Guangdong, China). Cohort 1 receives fresh-frozen human tissue samples of patients with gastric cancer primarily for 16S rRNA sequencing and qPCR analysis to investigate microbial community distribution and analyze progression-free survival (PFS). Cohort 2 involves human gastric cancer tissue microarray of formalin-fixed, paraffin-embedded samples, utilized mainly for *in situ* hybridization to detect *F. nucleatum* distribution and conduct overall survival (OS) analysis, including data from follow-ups exceeding 5 years. All patients were preoperatively diagnosed with gastric cancer and underwent radical resection. All tissue samples were isolated and frozen at −80°C or formalin-fixed and paraffin-embedded. This study was approved by the Institutional Review Board of the First Affiliated Hospital of Sun Yat-sen University and conducted according to the tenets of the Declaration of Helsinki. Each participant signed a consent form before participating in the study.

Animal studies

The 615, C57BL/6 (RRID: IMSR_JAX:000664), and BALB/c mice (RRID: MGI:2683685) were obtained from the Animal Experiment Center of Sun Yat-sen University and Youda (Guangzhou) Biotechnology Co., Ltd. and were raised in specific pathogen-free animal rooms. The Institutional Ethics Committee of the First Affiliated Hospital for Animal Studies approved the animal study protocols. The ARRIVE reporting guidelines were followed (18). The animal study was carried out in compliance with the guidance of the Animal Care Committee of the First Affiliated Hospital of Sun Yat-sen University [permit number: (2021)737]. The laboratory management personnel allocated the mice and cage placements using a random grouping method, thereby ensuring single blinding for the experiment operators. The research personnel randomly divided the mice into a control group and a treatment group. All mice were raised in a controlled, specific pathogen-free environment. The mice were humanely euthanized via cervical dislocation following anesthesia with isoflurane and subsequently dissected. The sample size was based on estimations by power analysis with a level of significance of 0.05. Animals without tumors were excluded from the study.

Primary gastric cancer model

The C57BL/6 mice (RRID: IMSR_JAX:000664) were randomly divided into two groups. The model group was orally gavaged with *H. pylori* SS1 (2×10^9 CFU in 200 μL PBS) 6 times in 2 weeks to establish successful colonization within the stomach. The experimental group was divided into three groups [*H.p*, *Escherichia coli*$^{H.\ p+}$ (*E. coli*$^{H.\ p+}$), and *F. n*$^{H.\ p+}$groups] 12 months after the last feeding of the bacterial solution. The *H.p, E. coli*$^{H.\ p+}$, and *F. n*$^{H.\ p+}$ groups were orally gavaged with PBS (200 μL), *DH5α* (2×10^8 CFU in 200 μL PBS), and *F. nucleatum* (ATCC 25586, 2×10^8 CFU in 200 μL PBS) strains for 6 months, respectively. In short, C57BL/6 male mice were orally gavaged with *H. pylori* SS1 ($n = 27$ for 12 months), *F. nucleatum* ($n = 9$ for 6 months), PBS ($n = 9$ for 12 months, $n = 9$ for 6 months), or *E. coli* ($n = 9$ for 6 months). We examined the color and texture of the stomach and perigastric lymph nodes (LN) following dissection. The perigastric tissues were separated from the stomach and removed. The appetizing tissue along the stomach axis curvature was cut, the gastric contents were washed, the gastric mucosa was exposed, and the mucosa was observed and separated into 4% paraformaldehyde and a cryoprotective solution.

Chronic gastritis model

The female C57BL/6 (RRID: IMSR_JAX:000664) conventional mice (6–8 weeks old) were randomly assigned into three groups: PBS (negative control), *E. coli* (positive control), and *F. nucleatum* (*F.n*). The PBS, *E. coli*, and *F.n* groups were orally gavaged with the PBS (200 μL), *DH5α* (2×10^8 CFU in 200 μL PBS), and *F. nucleatum* (2×10^8 CFU in 200 μL PBS) strains for 3 months.

Subcutaneous tumor xenograft model

In this model, bacteria were first retrieved from an anaerobic workstation, whereas *F. nucleatum* was washed off blood plates and

centrifuged at 4,000 *g* for 3 minutes to remove the supernatant. After washing once with PBS and resuspending, bacterial liquid OD600 absorbance was measured. When the OD600 value reached 1, the quantity of *F. nucleatum* was determined to be 10^9 CFU/mL. Subsequently, *F. nucleatum* was cocultured with gastric cancer cells at a density of multiplicity of infection (MOI) 100, using a culture medium without antibiotics. After coculturing for 4 hours, the cell culture medium was discarded, and the cells were washed twice with PBS before being cultured in complete growth medium containing nonpenetrating antibiotics for 24 to 48 hours. The cells were then retrieved from the 37°C incubator, and the cell pellets were collected at a centrifugal speed of 1,000 rpm/minute for 5 minutes. Bacterial precipitate was resuspended using PBS or serum-free medium. The cell suspension was then injected subcutaneously into BALB/C mice and immunocompetent 615 mice (the 615 mice strain was developed by crossing C57BL/6 and BALB/c mice, resulting in a hybrid strain with genetic characteristics from both parental strains). Around the fourth day of the formation of a subcutaneous tumor, an injection of bacterial suspension containing 5×10^7 CFU in 50 μL PBS was administered into or around the tumor. The 15-cm culture dish was used to cultivate the mouse forestomach carcinoma (MFC) and human MGC803 cell lines to construct a 615 and BALB/c mice subcutaneous tumor xenograft model at a density of 5×10^6 cells per mouse, with six mice per group. The cells were prepared before performing the animal experiments as follows. We injected 100 μL of the cell suspension into the right armpit/groin of nude mice using a 1-mL insulin injection needle, and the subcutaneous tumor formation in the mice was then observed. After 3 to 4 days, the long and short diameters of the subcutaneous tumors were measured twice a week using a Vernier caliper. The tumor volume under the short axis was calculated, and a growth curve for the tumor volume was drawn using the following formula: Mice were euthanized by cervical dislocation approximately 3 to 4 weeks later. The subcutaneous tumors in the axilla/groin of the mice were dissected, weighed, soaked in 4% paraformaldehyde, and fixed for subsequent experiments.

Tail vein–lung metastasis and footpad–popliteal LN metastasis model

A 615 mice/nude mouse tail vein–lung xenograft tumor model was constructed by injecting 1×10^6 cells per mouse, with 6 to 8 mice per group, and using a 15-cm dish to culture the MFC cell strain (luciferase-labeled) and human MGC803 gastric cancer cell line (luciferase-labeled). In the tail vein–pulmonary metastasis model, the mouse was fixed with clamps or a mortar, 100 μL of cell suspension was injected into the tail vein of the mouse using an insulin injection needle, and the vital signs were observed. The *in vivo* imaging systems (Lumina II, Xenogen Corp.) were used to capture bioluminescent images after 6 to 8 weeks. Mice were euthanized by cervical dislocation after images were taken, and the lungs were dissected and photographed, fixed with 4% paraformaldehyde, embedded in paraffin, sectioned, and stained with hematoxylin and eosin (H&E). The number of lung metastatic tumors was counted under a microscope (see below).

In the footpad–popliteal LN metastasis model, cells were prepared as described above and injected into the mouse footpad at 1×10^6 cells. Approximately 1 week after the growth of the footpad tumor, *F. nucleatum* suspension with 1% PBS solution was injected twice a week or injected with a 1×10^6 cell suspension (cocultured with *F. nucleatum*) one time, and bioluminescent images were captured after 4 to 6 weeks. Footpad tumors and popliteal LNs were dissected and removed, photographed, and fixed in 4% paraformaldehyde for subsequent experiments.

16S rRNA sequencing and data analysis

The gastric cancer tissue samples stored at −80°C were thawed. Subsequently, they were fully ground using a grinding bead homogenizer (BioSpec). The QIAamp PowerFecal DNA Kit (Qiagen) was used to extract microbial DNA from the resulting tissue pellets. Sequencing was performed on the MiSeq platform (Illumina) with the MiSeq Reagent Kit version 3 (Illumina). The off-machine data were split using MiSeq Reporter (Illumina). Using specific primers with barcodes, the V3–V4 region of the bacterial 16S rRNA gene was amplified with the primer pair 338F (5′-ACTCCTACGGGAGGCAGCAG-3′) and 806R (5′-GGACTACHVGGGTWTCTAAT-3′). A QuantiFluor fluorometer was used to quantify the PCR amplification product. The purified amplification product was mixed in the same amount, the sequencing connector was connected, the sequencing library was constructed, and the Illumina PE250 was sequenced on the machine (Supplementary Table S1).

Alpha diversity

Alpha diversity was applied in analyzing the complexity of species diversity for a sample through 14 indices, including richness, chao1, shannon_2, shannon_e, shannon_10, jost, jost1, simpson, dominance, equitability, robbins, berger_parker, reads, and buzas_gibson. All the indices in our samples were calculated with usearch-alpha_div (V10, http://www.drive5.com/usearch/), and rarefaction curve and rank abundance were calculated separately. The differences between groups were analyzed by alpha diversity index using R software. If there were only two groups, the Student *t* test or Wilcoxon rank-sum test was selected, but if there were more than two groups, the Kruskal–Wallis rank-sum test or one-way ANOVA was used.

Beta diversity

Beta diversity analysis was used to evaluate differences in species complexity among samples through nine algorithms, including bray_curtis, Euclidean, abund_jaccard, Canberra, chisq, chord, gower, weighted_unifrac, and unweighted_unifrac, using R software. Principal component analysis was performed to get principal coordinates and visualize complex and multidimensional data using the prcomp function in R software. Principal Coordinates Analysis (PCoA) and non-metric multidimensional scaling (NMDS) were displayed using the vegan package (RRID: SCR_011950) in R software. Sample cluster analysis was performed as an unweighted pair group method with arithmetic means method to interpret the distance matrix using average linkage based on the nine algorithms mentioned above. A distance heatmap was generated based on the results obtained from integrating the nine algorithms, followed by hierarchical clustering using the "hclust" function in the vegan package of R software.

Comparison between samples

Linear discriminant analysis (LDA) effect size (RRID: SCR_014609) was used to find the biomarker of each group based on a homogeneous OTU table. First, a nonparametric factorial Kruskal–Wallis sum-rank test was used to detect species with significant differences in abundance among different groups. Second, the Wilcoxon rank-sum test was used to judge the difference between the two groups. Finally, LDA was used to evaluate the impact of significant species (LDA score)

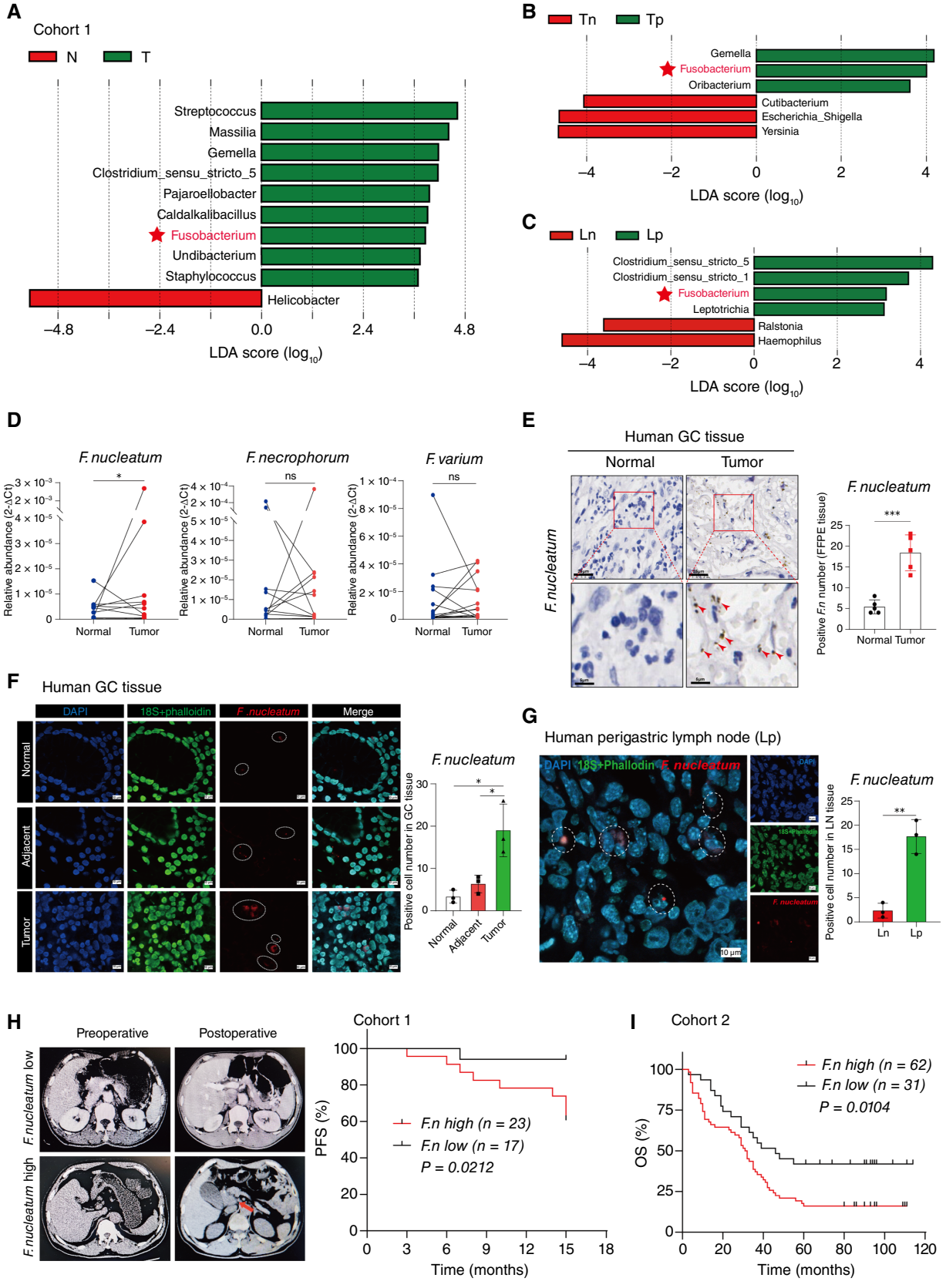
A
Cohort 1
N
T
Streptococcus
Massilia
Gemella
Clostridium_sensu_stricto_5
Pajaroellobacter
Caldalkalibacillus
Fusobacterium
Undibacterium
Staphylococcus
Helicobacter
−4.8
−2.4
0.0
2.4
4.8
LDA score (log10)
B
Tn
Tp
Gemella
Fusobacterium
Oribacterium
Cutibacterium
Escherichia_Shigella
Yersinia
−4
−2
0
2
4
LDA score (log10)
C
Ln
Lp
Clostridium_sensu_stricto_5
Clostridium_sensu_stricto_1
Fusobacterium
Leptotrichia
Ralstonia
Haemophilus
−4
−2
0
2
4
LDA score (log10)
D
F. nucleatum
F. necrophorum
F. varium
Relative abundance (2-ΔCt)
*
ns
ns
Normal
Tumor
E
Human GC tissue
Normal
Tumor
F. nucleatum
F. nucleatum
***
Positive F.n number (FFPE tissue)
Normal Tumor
F
Human GC tissue
DAPI
18S+phalloidin
F. nucleatum
Merge
Normal
Adjacent
Tumor
F. nucleatum
Positive cell number in GC tissue
*
*
Normal
Adjacent
Tumor
G
Human perigastric lymph node (Lp)
DAPI 18S+Phallodin F. nucleatum
10 μm
F. nucleatum
Positive cell number in LN tissue
**
Ln
Lp
H
Preoperative
Postoperative
F.nucleatum low
F.nucleatum high
Cohort 1
PFS (%)
F.n high (n = 23)
F.n low (n = 17)
P = 0.0212
Time (months)
I
Cohort 2
OS (%)
F.n high (n = 62)
F.n low (n = 31)
P = 0.0104
Time (months)

by setting the LDA score ≥2 and obtaining the biomarkers in different groups. If there were only two groups, Student *t* test, Wilcox rank sum test, Wilcoxon signed rank test or Welch *t* test was used to evaluate by R software, and corrected though FDR. But if there were more than two groups, Kruskal Wallis rank sum test or one-way ANOVA was used to evaluate by R software, and corrected though FDR.

Bulk RNA-seq and data analysis

RNA sequencing (RNA-seq) was performed on an Illumina HiSeq 3000 platform (Shanghai Genergy BioTech), following the manufacturer's instructions. Data were analyzed according to the TopHat-HTSeq-DeSeq2 framework. The raw RNA sequence data were deposited in the Gene Expression Omnibus (GEO) database (RRID: SCR_005012). Differentially expressed genes (DEG) between control and *F. nucleatum*–infected groups in bulk transcriptomic data were identified using DESeq2 (RRID: SCR_015687).

Single-cell RNA-seq and data analysis

BD Rhapsody system was used to capture the transcriptomic information of the single cells. Single-cell capture was achieved by random distribution of a single-cell suspension across >200,000 microwells through a limited dilution approach. Beads with oligonucleotide barcodes were added to saturation so that a bead was paired with a cell in a microwell. Cell lysis buffer was added to hybridize polyadenylated RNA molecules to the beads. Beads were collected into a single tube for reverse transcription. Upon cDNA synthesis, each cDNA molecule was tagged on the 5′ end (i.e., the 3′ end of an mRNA transcript) with a unique molecular identifier and cell label indicating its cell of origin. Whole-transcriptome libraries were prepared using the BD Rhapsody single-cell whole-transcriptome amplification workflow. In brief, second-strand cDNA was synthesized, followed by ligation of the whole transcriptome analysis (WTA) adaptor for universal amplification. A total of 18 cycles of PCR were used to amplify the adaptor-ligated cDNA products. Sequencing libraries were prepared using random priming PCR of the whole-transcriptome amplification products to enrich the 3′ end of the transcripts linked with the cell label and unique molecular identifier and were quantified using a High Sensitivity DNA chip (Agilent) on a Bioanalyzer 2200 and the Qubit High Sensitivity DNA assay (Thermo Fisher Scientific). All libraries were sequenced by DNBSEQ-T7 Sequencer (MGI) on a 150-bp paired-end run.

GO analysis

To elucidate the biological implications of the DEGs and marker genes, gene ontology (GO) analysis was performed. GO annotations were downloaded from NCBI (http://www.ncbi.nlm.nih.gov/; RRID: SCR_006472), the Gene Ontology database (http://www.geneontology.org/), and UniProt (http://www.UniProt.org/; RRID: SCR_002380). Fisher's exact test was applied to identify the significant GO categories, and an FDR was used to correct the *P* values.

Pathway analysis

Pathway analysis was used to explore the significant pathways of the DEGs and marker genes based on the Kyoto Encyclopedia of Genes and Genomes (KEGG) database (RRID: SCR_001120). Fisher's exact test was used to identify significant pathways, and the threshold of significance was defined by the *P* value and FDR.

Gene set enrichment analysis

To characterize the relative activation of a given gene set, we performed QuSAGE (2.16.1) analysis (RRID: SCR_024255).

Cell–cell communication analysis

To enable a systematic analysis of cell–cell communication molecules, we applied cell communication analysis based on the CellPhoneDB (version 2.0; https://github.com/Teichlab/cellphonedb; RRID: SCR_017054), a public repository of ligands, receptors, and their interactions (19). Membrane, secreted, and peripheral proteins of the cluster of different time points were annotated. Significant mean and cell communication significance (*P* value < 0.05) were calculated based on the interaction and the normalized cell matrix achieved by Seurat normalization. Cell communication analysis was performed using the R package CellChat (version 1.1.3; RRID: SCR_021946) with default parameters. The CellChat DB human was used for analysis. All two groups of samples were normalized together, and then each group was extracted, analyzed, and compared in parallel. This is with the assumption that they were sharing cell types.

Differential gene expression analysis

To identify differentially expressed genes among samples, the function FindMarkers with the Wilcoxon rank-sum test algorithm was used under the following criteria: (i) $\log_2$ fold change > 0.25, (ii) *P* value < 0.05, and (iii) minutes.pct > 0.1, which was more conducive to obtaining different functional genes among samples.

Cell lines and culture

Human gastric cancer cell lines (AGS, RRID: CVCL_0139; MKN1, RRID: CVCL_1415; MKN28, RRID: CVCL_1416; and MGC803, RRID: CVCL_5334) and mouse gastric cancer cell lines (MFC, RRID: CVCL_5J48) were purchased from the Shanghai Branch of the Chinese Academy of Sciences. AGS cells were cultured in DMEM/F-12 (Gibco) supplemented with 10% FBS (Israel Bioindustries) and 1% antibiotics (penicillin/streptomycin, Gibco) at 37°C with 5% CO_2. MKN1/MKN28/MFC cells were cultured in RPMI 1640 (Gibco) supplemented with 10% FBS and 1% antibiotics at 37°C with 5% CO_2. MGC803 cells were cultured in DMEM (Gibco) supplemented with 10% FBS and 1% antibiotics at 37°C with 5% CO_2. All cell lines were confirmed negative for mycoplasma contamination using PCR.

Figure 1.

F. nucleatum is significantly enriched in patients with gastric cancer with lymph node metastasis. **A,** LDA score of bacterial abundance between gastric cancer tissues (T) and normal (N) tissues at the genus level. The bacteria with values of $\log_{10}$ (LDA score) >3 are shown ($n = 40$). **B,** The LDA plot was used to compare the bacterial abundance in the primary lesions of patients with gastric cancer with or without LN metastasis. Tn, tumor tissues without lymph node metastasis; Tp, tumor tissues with lymph node metastasis. **C,** The LDA plot was used to compare the bacterial abundance in the perigastric LNs of patients with gastric cancer with or without LN metastasis. **D,** qRT-PCR analysis indicated the abundance of *F. nucleatum* in gastric cancer tissues compared with normal tissues ($n = 14$). FFPE, formalin-fixed, paraffin-embedded. **E,** *In situ* hybridization demonstrates the localization and expression levels of *F. nucleatum* in gastric cancer (GC) tissues. **F,** FISH analysis demonstrated an enrichment of *F. nucleatum* within the primary lesion of gastric cancer. **G,** FISH results indicated the detection of *F. nucleatum* within the LNs in patients with metastatic gastric cancer. **H,** Left, representative CT scans from a patient with gastric cancer and postoperative recurrence (high *F. nucleatum*, metastasis). Right, survival curve displayed the PFS rates of patients with gastric cancer at different expression levels of *F. nucleatum* ($n = 40$). **I,** The OS of patients with lower or higher *F. nucleatum* abundance in gastric cancer ($n = 93$). Log-rank test was used. Data are presented as mean ± SEM. *, $P < 0.05$; **, $P < 0.01$; ***, $P < 0.001$; ns, not significant.

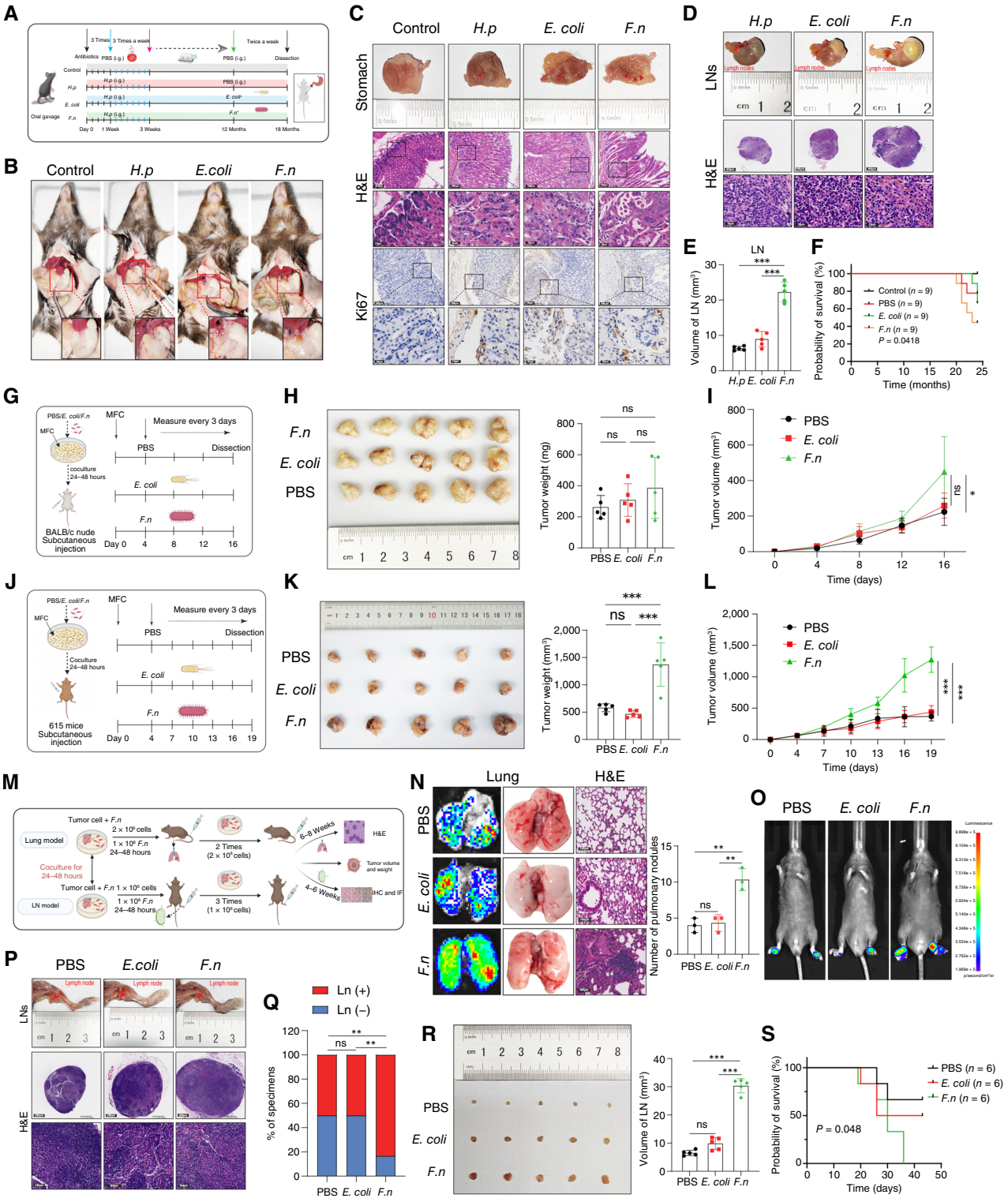

Figure 2.

F. nucleatum promotes the malignant progression of gastric cancer. **A,** C57BL/6 male mice were orally gavaged with *H. pylori* SS1 ($n = 27$ for 12 months), *F. nucleatum* ($n = 9$ for 6 months), PBS ($n = 9$ for 12 months; $n = 9$ for 6 months), or *E. coli* ($n = 9$ for 6 months). i.g, intragastric gavage. **B,** *In situ* image of the stomach of mice infected with *F. nucleatum*, *H. pylori*, or *E. coli*. **C,** Representative H&E staining images of the stomach of mice demonstrated higher atypical hyperplasia in the gastric mucosa of the mice in the *F. nucleatum*-positive (*F.n*$^{+}$) group. **D** and **E,** Representative macroscopic images and H&E staining images of peripheral gastric lymph nodes in the primary gastric cancer model. H&E results showed the status of LN infiltration. **F,** (*Continued on the following page.*)

Bacterial strain and culture conditions

The *F. nucleatum* strain was purchased from Guangdong Institute of Microbiology and was obtained from ATCC (*Fusobacterium nucleatum* subsp. *nucleatum*, ATCC 25586). In brief, *F. nucleatum* was inoculated, cultured, and subcultured on a blood plate (Huankai Biotechnology); then, it was cultured in the AS-580 chamber of the anaerobic bacteria system at 37°C with 10% CO_2, 10% H_2, and 80% N_2. The *E. coli* strain, *DH5α* (Invitrogen), was propagated in Luria-Bertani (BD Biosciences, Difco) medium aerobically at 37°C.

Bacterial and cell coculture

We generally chose a six-well plate as the coculture system. Tumor cells needed to adhere to the wall and reach 70% to 90% density before coculture experiments. We collected *F. nucleatum* during the logarithmic growth period and adjusted the suspension concentration to 1×10^9 CFU/mL for interaction experiments. MOI was used to examine the proportion of bacteria and cancer cells. A MOI of 100 is often used as a prerequisite for *in vivo* and *in vitro* experiments.

Antibiotics experiment

Gastric cancer cells and *F. nucleatum* were cocultivated in a medium containing ampicillin + gentamicin (200 + 200 μg/mL) or doxycycline (10 μg/mL) and cultured at 37°C overnight; then, they were centrifuged to obtain the supernatant and cell pellets. Subsequently, they were streaked on the blood plate and cultured in an anaerobic workstation. The combination of ampicillin and gentamicin was used to remove extracellular bacteria, and doxycycline was used to remove both extra- and intracellular bacteria.

Sample preparation for electron microscopy

Animal tissue samples

Lymph nodes were dissected and separated from the popliteal fossa of mice and then immediately placed in a PBS-containing well plate for cleaning. Subsequently, they were drained on clean paper, immediately placed into a 2.5% glutaraldehyde electron microscope fixation solution, and fixed at room temperature for 30 minutes (attention was paid to protect the sample from light at this phase). Finally, the samples were transported on ice to a 4°C refrigerator for storage.

Cells

Cells were taken out of the incubator (the cell density generally did not exceed 70%), and the medium was discarded. The electron microscope solution at room temperature was added to the samples. The samples were fixed at room temperature and protected from light for 5 minutes. A cell scraper was used to gently scrape the cells in one direction, avoiding back-and-forth movements to prevent cell damage. The samples were centrifuged at 2,000 *g* for 5 minutes, and the cell pellets after centrifugation were about the size of a mung bean. The original electron microscope fixative was discarded, and a new one was added. The cell mass was blown off and resuspended. For storage, the samples were fixed for 30 minutes at room temperature in the dark and transferred to 4°C on ice.

Fluorescence confocal imaging

A 24-well plate was prepared, in which gastric cancer cells were cocultured with *F. nucleatum*/*E. coli* for 24 hours. The cell supernatant was discarded, and the cells were washed two to three times with a 1% PBS solution. Endocytosis detection dye (21217, Protonex Green 500 Dextran, working solution prepared by mixing 20 μL stock solution and 980 μL 1% PBS solution) was added to the cells (5–10 μL/well). A fluorescence microscope or confocal microscope was used to take images, and the changes in gastric cancer cell membrane structure in living cells and cell slides were observed.

Transwell assay

We cultured 50,000 cells in the top of the transwell chamber (for migration analysis; Corning Costar), with 300 μL of serum-free medium, whereas the chamber was outside the 24-well plate. Then, 600 μL of culture medium containing 10% FBS was added. After 16 to 72 hours of coculturing, the migrated or invaded cells were stained with crystal violet and counted under a microscope (Olympus).

FISH

Using the fluorescent carrier Cy3-labeled *F. nucleatum* 16S rRNA probe (5-/Cy3/CTTGTAGTTCCGCCTACCTC-3), the colonization of bacteria in human and mouse tissues was detected using fluorescence *in situ* hybridization (FISH). A nonspecific complement probe (5-/Cy3/CTTGTAGTTCCGCCTACCTC-3) served as a control for the hybridization method. A FISH kit (Gimma Gene) was used to detect bacterial localization and enrichment in tissues and cells. A fluorescent confocal microscope and an inverted/upright fluorescence microscope were used to collect images.

RT-qPCR

Total RNA was extracted using TRIzol reagent (Takara), followed by cDNA synthesis using the Master Mix cDNA Synthesis Kit (Accurate Biotechnology). Quantification of specific RNA was carried out using SYBR Green I (Accurate Biotechnology). The qPCR protocol was executed using a LightCycler 480 II (Roche). Fold change was determined employing the relative quantification method ($2^{-\Delta\Delta Ct}$). The qPCR primer sequences are detailed in Supplementary Table S2.

Flow cytometry

The fresh spleen and tumor tissues were extracted from 615 mice, grinding them into tissue fragments. The samples were then

(*Continued*.) The survival curves illustrate the survival times and proportions of mice in different groups. **G,** In this model, the PBS ($n = 5$), *E. coli* ($n = 5$), and *F. nucleatum* ($n = 5$) were cocultured with gastric cancer cells, and the cell suspension was then injected subcutaneously into BALB/C mice. **H** and **I,** The macroscopic images of tumor tissues and growth curves displaying the growth status of subcutaneously xenografted tumor models in BALB/c nude mice following *F. nucleatum* infection. **J,** Construction diagram for the subcutaneous tumor model in 615 mice. **K** and **L,** The macroscopic images of tumor tissues and growth curves displaying the growth status of subcutaneously xenografted tumor models in 615 mice following *F. nucleatum* infection. **M,** The model construction pattern of the mouse tail vein–lung metastasis model and popliteal LN metastasis model. IF, immunofluorescence. **N**, Representative *in vivo* imaging system staining, macroscopic images, and H&E staining of lung tissues from mice in the tail vein–lung metastasis model. **O,** The *in vivo* imaging systems revealed the fluorescence of popliteal LNs within the mouse popliteal LN metastasis model. **P,** The popliteal LN metastasis anatomy and LN tissue and the H&E staining of popliteal LNs in mice. **Q,** Representative quantification of LN-negative and LN-positive tissues in PBS, *E. coli*, and *F. nucleatum* groups. **R**, The LN volume contrast histogram. **S,** The survival curve of mice with implanted footpad lymph node metastasis model. Data are presented as mean ± SEM. *, $P < 0.05$; **, $P < 0.01$; ***, $P < 0.001$; ns, not significant. **A**, **G**, **J**, and **M**, Created with BioRender.com. Zhang, T. (2025), https://BioRender.com/r65m917.

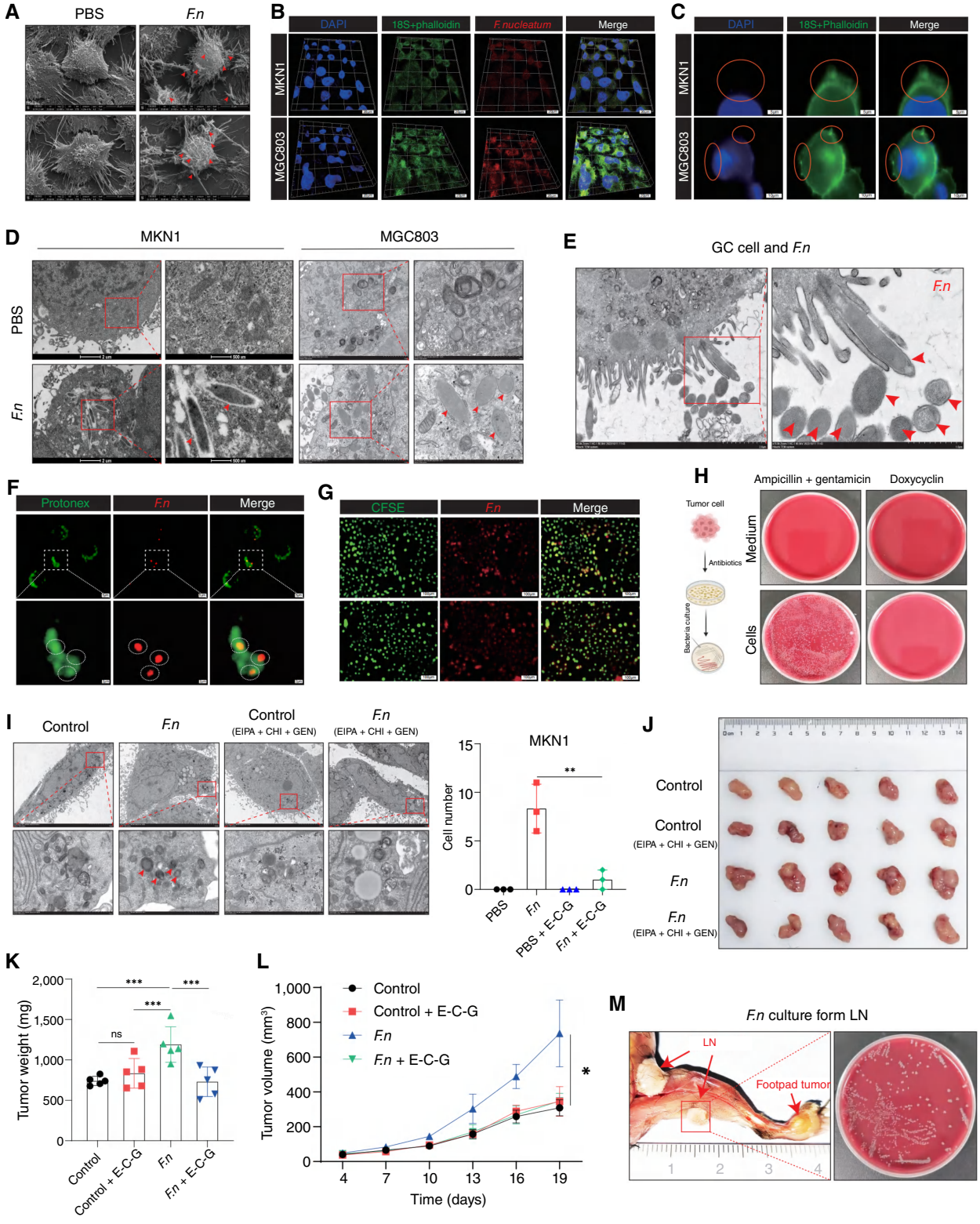

Figure 3.

F. nucleatum invades gastric cancer cells and establishes intracellular colonization. **A,** Representative SEM images of MKN1 cells after coculture with *F. nucleatum*. **B,** Representative 3D fluorescence confocal images of *F. nucleatum* infection in gastric cancer cells. **C,** Representative confocal images of cystic protrusions and folds on the surface of gastric cancer cells infected by *F. nucleatum*. **D,** Representative TEM images of gastric cancer cells (*Continued on the following page.*)

digested with trypsin to create a cell suspension, which was filtered through a 70-micron mesh to remove tissue debris. Red blood cells were eliminated using a lysis buffer, followed by cell counting. The samples were treated with 1:1,000 diluted Fixable Viability Stain prepared in 1× PBS and incubated at 4°C for 20 minutes in the dark. Subsequently, the cells were washed 1 to 2 times with staining buffer containing 1% FBS and resuspended. Fc receptor blocking solution (less than 2 μL per test) was added to each tube, followed by a 15-minute incubation in the dark. Antibodies were then mixed proportionally and added to the staining buffer; each antibody was quickly mixed upon addition to prevent accumulation, with a subsequent 15-minute incubation at room temperature. After washing and centrifugation (300 *g* for 5 minutes), the samples were analyzed using flow cytometry. The samples were divided into "blank," "single staining," and "mixed staining" groups (50 μL of the cell suspension was added to each tube, aliquoted into tubes, and incubated). The flow antibody was added according to the antibody instructions and incubated for 1 hour (protected from light). The samples were resuspended in 300 μL PBS and tested on the flow cytometer. Debris were removed by gating for forward and side scatter in the tumor cell suspension. Recognition of neutrophil ($CD45^+$ $CD11b^+$ $Ly6G^+$), $CD4^+$ T cell ($CD45^+$ $CD3^+$ $CD4^+$), $CD8^+$ T cell ($CD45^+$ $CD3^+$ $CD8^+$), and NK cell ($CD45^+$ $CD3^-$ $NK1.1^+$) was performed. Tumor cell suspensions were gated for forward and side scatter and depleted before recognition of neutrophil ($CD45^+$ $CD11b^+$ $Ly6G^+$) debris. Neutrophils were stained with anti-CD45, CD11b, and anti-CD66b. The CytoFLEX/BD LSRFortessa flow cytometer (BD Biosciences) was used for analysis. FlowJo (RRID: SCR_008520) software was used for data analysis. The antibodies are detailed in Supplementary Table S3.

Western blots

Protein extraction was conducted using Tissue Extraction Reagent (Thermo Fisher Scientific) supplemented with protease inhibitors (Roche) and PhosSTOP (Roche). Subsequently, the captured image was analyzed using Image Lab software (version 5.2.1, Bio-Rad). The expressed protein levels were normalized to GAPDH (Proteintech, Cat. # CL488-60004, RRID: AB_2919223). The antibodies are detailed in Supplementary Table S3.

H&E staining

The tissue sections were dewaxed, as described above. Subsequently, the sections were washed twice with PBS to remove residual ethanol. The slides were then stained with hematoxylin according to the IHC procedure. When the tap water turned blue, the slides were stained with the eosin solution (Soleibao). After 5 minutes, the staining process was stopped with a tap-water wash. The slides were then left in a fume hood to air-dry naturally. Afterward, the slides were sealed with neutral resin. The slide scanning system was used for archiving.

IHC staining

The IHC immunoreactive score of Remmele and Stegner was calculated as the sum of positive stained tumor cells and staining intensity. Briefly, the percentage of positive staining was scored as 1 (<10%, negative), 2 (11%–55%, sporadic), 3 (56%–80%, focal), or 4 (>81%, diffuse). Staining intensity was scored as 0 (no staining), 1 (weak staining), 2 (moderate staining), or 3 (strong staining). The median immunoreactive score of Remmele and Stegner was used to determine whether the indicated molecule was expressed strongly or weakly immunohistochemically. The slides were subsequently analyzed using a KF-PRO Slide Scanner (KFbio). Five fields from each slide were randomly selected for imaging, and the resulting images were processed using ImageJ (RRID: SCR_003070). The antibodies are detailed in Supplementary Table S3.

Immunofluorescence staining

Fresh tissues were fixed in a 4% neutral buffered formalin solution and subsequently embedded in paraffin. Multiplex immunofluorescence (MIF) staining was conducted using a kit from Wuhan Servicebio Technology Co., Ltd. Deparaffinization and rehydration followed after melting tissue sections (8 μm) at 60°C for 1 hour. Microwave incubation was used for heat-mediated retrieval of antigens from citrate acid buffer (pH 6.0). After the addition of blocking buffer for 10 minutes, the sections were incubated with primary antibodies against CD8 (GB114196, RRID: AB_3064847), CD16 (GB113963, RRID: AB_3665881), Ly6G (GB11229, RRID: AB_2814689), CD3 (GB111337, RRID: AB_3665880), CD56 (GB112671, RRID: AB_3665882), CD49b (BioLegend, cat. #103501, RRID: AB_313024), NK1.1 (BioLegend, cat. #108714, RRID: AB_389364), and FOXP3 (GB112325, RRID: AB_2922969). The sections were incubated with horseradish peroxidase–conjugated secondary antibodies for 10 minutes at room temperature. Stained signals were further amplified using tyramide signal amplification reagents (G1231, G1223, G1232, and G1222, Wuhan Servicebio Technology Co., Ltd.), and the stained signals were further amplified. Finally, 4′,6-diamidino-2-phenylindole was used to stain the nuclei. A fluorescence imaging system was used to scan the stained slides (Olympus/BX63). The antibodies are detailed in Supplementary Table S3.

ELISA

Cytokine expression levels, including IL17A, IL1β, IL8, G-CSF, and GM-CSF, were identified through the use of an ELISA kit in both the cell culture supernatant and mouse serum (COIBO).

Statistical analysis

Between-group differences in quantitative data were analyzed using the unpaired or paired Student *t* test, Mann–Whitney *U* test, or Dunnett *t* test, where appropriate. Among-group differences were analyzed using one-way ANOVA. The effects of clinical parameters were estimated by univariate or multivariate Cox proportional

(*Continued*.) after coculture with *F. nucleatum*. The higher magnification images demonstrate the invasion of gastric cancer cells by *F. nucleatum*. **E,** Representative TEM images show that gastric cancer (GC) cell membranes extended tentacles to wrap *F. nucleatum*. **F,** Representative living cell fluorescence images of *F. nucleatum* being endocytosed by gastric cancer cells. **G,** CFSE staining was employed to demonstrate the impact of *F. nucleatum* infection on the viability of gastric cancer cells. **H,** Antibiotic experiments verified the intracellular survival status of *F. nucleatum*. **I,** The application of endocytosis inhibitors led to a noteworthy reduction in the quantity of *F. nucleatum* that invaded gastric cancer cells. **J,** The macroscopic image of the subcutaneous tumor xenograft model with endocytosis inhibition. **K,** The specific values of tumor tissue weights for different groups of mice in a histogram. **L,** Growth curves displaying tumor volumes. **M,** Dissect the popliteal LN tissue of the mouse foot pad LN metastasis model for culture to confirm the presence of viable *F. nucleatum* in the LNs. Data are presented as mean ± SEM. *, $P < 0.05$; **, $P < 0.01$; ***, $P < 0.001$; ns, not significant. CHI, chlorpromazine; GEN, genistein; E-C-G, EIPA-chlorpromazine-genistein.

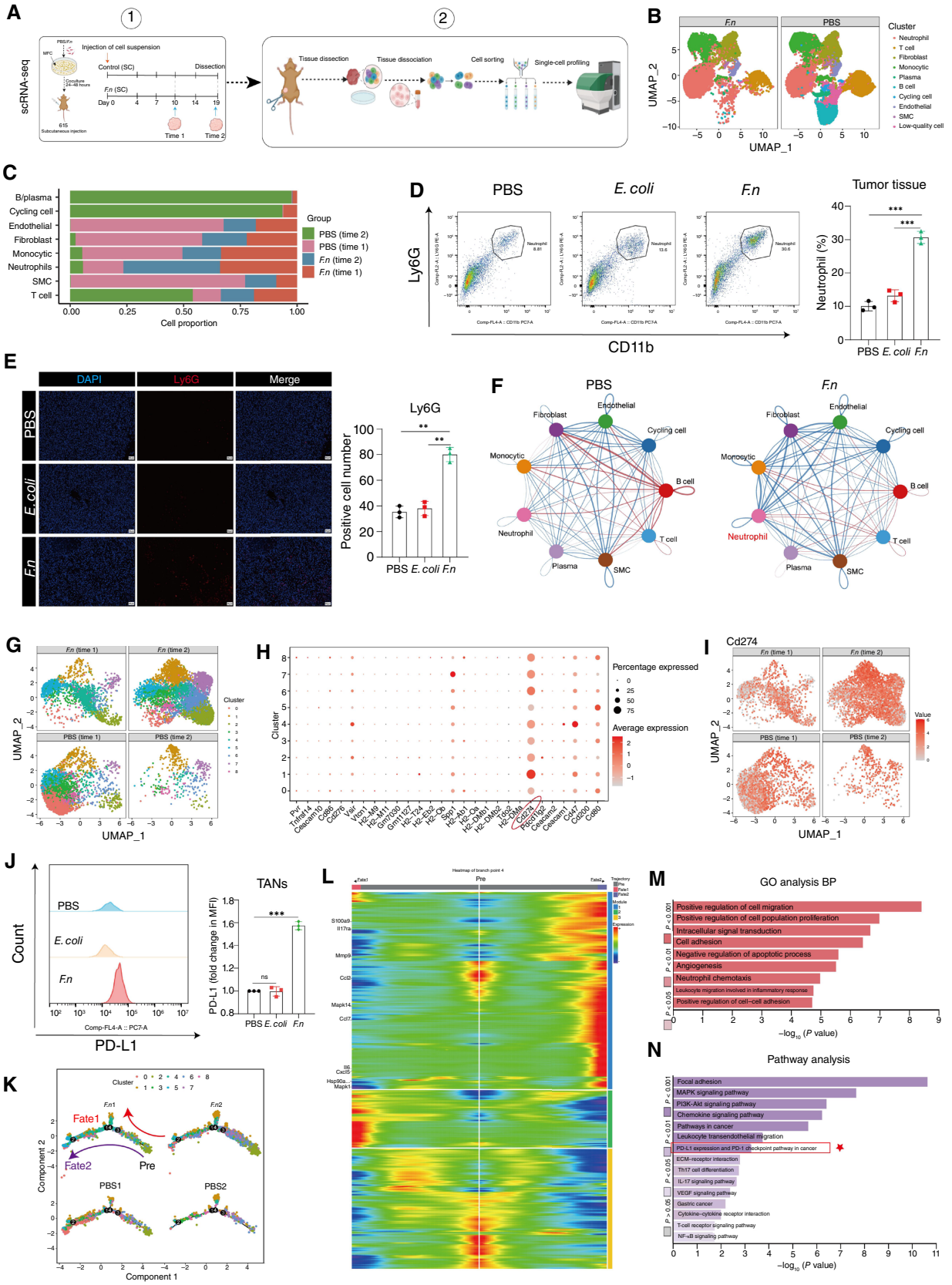
A
scRNA-seq
Injection of cell suspension
Control (SC)
Dissection
F.n (SC)
Day 0
Time 1
Time 2
Tissue dissection
Tissue dissociation
Cell sorting
Single-cell profiling
B
F.n
PBS
Cluster
Neutrophil
T cell
Fibroblast
Monocytic
Plasma
B cell
Cycling cell
Endothelial
SMC
Low-quality cell
UMAP_1
UMAP_2
C
B/plasma
Cycling cell
Endothelial
Fibroblast
Monocytic
Neutrophils
SMC
T cell
Group
PBS (time 2)
PBS (time 1)
F.n (time 2)
F.n (time 1)
Cell proportion
D
PBS
E. coli
F.n
Ly6G
CD11b
Tumor tissue
Neutrophil (%)
E
DAPI
Ly6G
Merge
PBS
E.coli
F.n
Positive cell number
F
PBS
F.n
Endothelial
Fibroblast
Cycling cell
Monocytic
B cell
Neutrophil
T cell
Plasma
SMC
G
F.n (time 1)
F.n (time 2)
PBS (time 1)
PBS (time 2)
Cluster
UMAP_1
UMAP_2
H
Cluster
Percentage expressed
Average expression
I
Cd274
Value
J
PBS
E.coli
F.n
Count
PD-L1
TANs
PD-L1 (fold change in MFI)
ns
K
Cluster
Fate1
Fate2
Pre
PBS1
PBS2
Component 1
Component 2
L
Pre
Fate1
Fate2
M
GO analysis BP
Positive regulation of cell migration
Positive regulation of cell population proliferation
Intracellular signal transduction
Cell adhesion
Negative regulation of apoptotic process
Angiogenesis
Neutrophil chemotaxis
Leukocyte migration involved in inflammatory response
Positive regulation of cell–cell adhesion
−log10 (P value)
N
Pathway analysis
Focal adhesion
MAPK signaling pathway
PI3K-Akt signaling pathway
Chemokine signaling pathway
Pathways in cancer
Leukocyte transendothelial migration
PD-L1 expression and PD-1 checkpoint pathway in cancer
ECM–receptor interaction
Th17 cell differentiation
IL-17 signaling pathway
VEGF signaling pathway
Gastric cancer
Cytokine–cytokine receptor interaction
T-cell receptor signaling pathway
NF-κB signaling pathway
−log10 (P value)

hazards regression analysis. Kaplan–Meier OS curves were generated and compared with the log-rank test. A Venn diagram was used to show flora selection, with *F. nucleatum* as the dominant flora in the primary gastric cancer and LN tissues simultaneously. Linear discriminant analysis of effect size and phylogenetic tree analysis were performed to screen significant bacteria in primary gastric cancers and LNs. All P values were two-tailed, and $P < 0.5$ was considered significant. Statistical analyses were conducted using IBM SPSS Statistics 23.0 (RRID: SCR_002865) and GraphPad Prism 9.0 software (RRID: SCR_002798).

Data availability

The raw sequence data reported in this paper, including the RNA-seq and 16s rRNA-seq data, have been deposited in the Genome Sequence Archive (Genomics, Proteomics & Bioinformatics 2021) in National Genomics Data Center (Nucleic Acids Res 2022), China National Center for Bioinformation/Beijing Institute of Genomics, Chinese Academy of Sciences (Project number: PRJCA035816, GSA-Human: HRA010338 and HRA010335, GSA: CRA022889) that are publicly accessible at https://ngdc.cncb.ac.cn/gsa-human and https://ngdc.cncb.ac.cn/gsa (20, 21). The raw data download can be requested according to the Genome Sequence Archive's instructions, and all requests for data will be approved after review by its Data Access Committee. The raw data of single-cell RNA-seq (scRNA-seq) can be accessed in the GEO database under the accession number GSE264532. The bulk RNA-seq data and clinical information of The Cancer Genome Atlas (TCGA) cohorts and GEO cohorts were obtained from the Genomic Data Commons Data Portal (https://portal.gdc.cancer.gov/), Timer 2.0 (https://timer.cistrome.org), GEPIA 2.0 (http://gepia2.cancer-pku.cn/#analysis), and Kaplan–Meier Plotter (https://kmplot.com/analysis/). All data generated in this study are available from the corresponding author upon request.

Results

F. nucleatum is significantly enriched in patients with gastric cancer with LN metastasis

To identify key microbes linked to gastric cancer progression, we analyzed the tissue microbiome of normal gastric mucosa, cancer, and LN of patients with gastric cancer using 16S rRNA amplicon sequencing, qRT-PCR, and FISH (cohort 1, $n = 40$). All examinations revealed that *Fusobacterium*, especially *F. nucleatum*, was highly enriched in gastric cancer lesions compared with normal tissue, particularly in patients with LN metastasis, suggesting a potential association between *F. nucleatum* and the engraftment process of gastric cancer cells (**Fig. 1A–F**; Supplementary Fig. S1A and S1B; Supplementary Tables S4–S6). Furthermore, both the 16S rRNA amplicon and FISH results indicated that an even higher *F. nucleatum* enrichment score was accumulated in the perigastric LNs (**Fig. 1G**; Supplementary Fig. S1C and S1D). Furthermore, patients with higher *F. nucleatum* enrichment scores had poorer PFS in cohort 1 and OS in cohort 2 ($n = 93$). In patients with *F. nucleatum* positivity, the median survival period was 31.5 months, whereas in patients with *F. nucleatum* negativity, it was 46 months (Supplementary Table S7). The CT/PET-CT imaging examination indicated that patients with gastric cancer with higher *F. nucleatum* enrichment scores were more likely to experience recurrence and metastasis after surgery. Moreover, the clinical data correlation analysis in cohort 2 revealed that patients with higher *F. nucleatum* enrichment scores exhibited increased T, N, and tumor–node–metastasis staging levels (**Fig. 1H** and **I**; Supplementary Fig. S1E; Supplementary Tables S8 and S9). These data indicated a close association between *F. nucleatum* and gastric cancer malignant progression.

F. nucleatum colonizes gastric mucosa and promotes malignant progression from gastritis to gastric cancer in mice

To investigate *F. nucleatum's* role in gastric cancer malignant progression, we first induced a primary gastric cancer model by orally gavaging *H. pylori* into C57BL/6 mice for 12 months, followed by gavaging with *F. nucleatum* to estimate its effect on gastric mucosa dysplasia and LNs metastasis. The *F. nucleatum*–infected mice displayed exacerbated progression of gastric carcinogenesis compared with those infected with *E. coli*. H&E staining demonstrated marked atypical hyperplasia, characterized by enlarged nuclei in glandular cells, varying sizes, disrupted polarity, disordered arrangement, and prominent nucleoli. IHC staining revealed higher Ki67 expression in *F. nucleatum*–infected mice (**Fig. 2A–C**; Supplementary Fig. S2A). Perigastric LNs in the *F. nucleatum*–infected mice exhibited significant enlargement, a color change to gray, and a hardened texture; further H&E staining revealed tumor cell infiltration (**Fig. 2D** and **E**). Survival times and OS were substantially shorter in *F. nucleatum*–infected mice (**Fig. 2F**).

To investigate the colonization ability of *F. nucleatum* in the gastric mucosal epithelium, gastric mucosal tissues from mice were dissected. Subsequently, microbial culturing was carried out under anaerobic conditions, and the bacterial strains were identified through mass spectrometry analysis. The results indicated the successful cultivation of *F. nucleatum* strains from the gastric mucosal tissues (Supplementary Fig. S2B and S2C). To clarify *F. nucleatum*'s impact on normal gastric mucosa, we administered *F. nucleatum* alone by gavage for 3 months. Compared with *E. coli*–infected mice, *F. nucleatum*–infected mice exhibited more severe manifestations of chronic and atrophic gastritis in the gastric mucosa (Supplementary

Figure 4.

F. nucleatum–infected gastric cancer cells induce TAN recruitment and differentiation. **A,** Overview of experiment design in scRNA-seq. **B,** The main cell types and clusters annotated by known cell lineages in PBS and *F. nucleatum* (*F.n*) samples are illustrated by Uniform Manifold Approximation and Projection (UMAP) plots. **C,** Bar plot showing a comparison of the proportions of the main cell types between PBS 1, PBS 2, *F.n*1, and *F.n*2. Among them, 1 and 2 represent different periods. **D,** Flow cytometry results showing the expression level of the neutrophil marker protein CD11b and Ly6G in subcutaneous tumors of mice. **E,** MIF showing the expression level of Ly6G in subcutaneous tumors of mice. **F,** Circle diagram demonstrating the interaction between different cell types in different groups. **G,** UMAP plot showing the distributions of these neutrophil clusters in different groups. **H,** Bubble plot illustrating the mean expression levels of immune checkpoint inhibition–related genes across distinct TAN clusters. **I,** UMAP plot showing the expression of CD274 (PD-L1) in different samples. **J,** The mean fluorescence intensity (MFI) analysis of flow cytometry revealed the expression level of PD-L1 within TANs in mice. **K,** The single-cell trajectory plots by Monocle demonstrating the reconstructed developmental path of tumor cells from neutrophils. **L,** Heatmap showing the expression of genes in a branched-dependent manner. Each row represents the dynamic expression of a gene. **M** and **N,** Bar chart displaying the results of GO and KEGG enrichment analysis on genes of corresponding clusters in **J**. Data are presented as mean ± SEM. **, $P < 0.01$; ***, $P < 0.001$; ns, not significant. BP, biological progress; SMC, smooth muscle cell. **A**, Created with BioRender.com. Zhang, T. (2025), https://BioRender.com/d33a784.

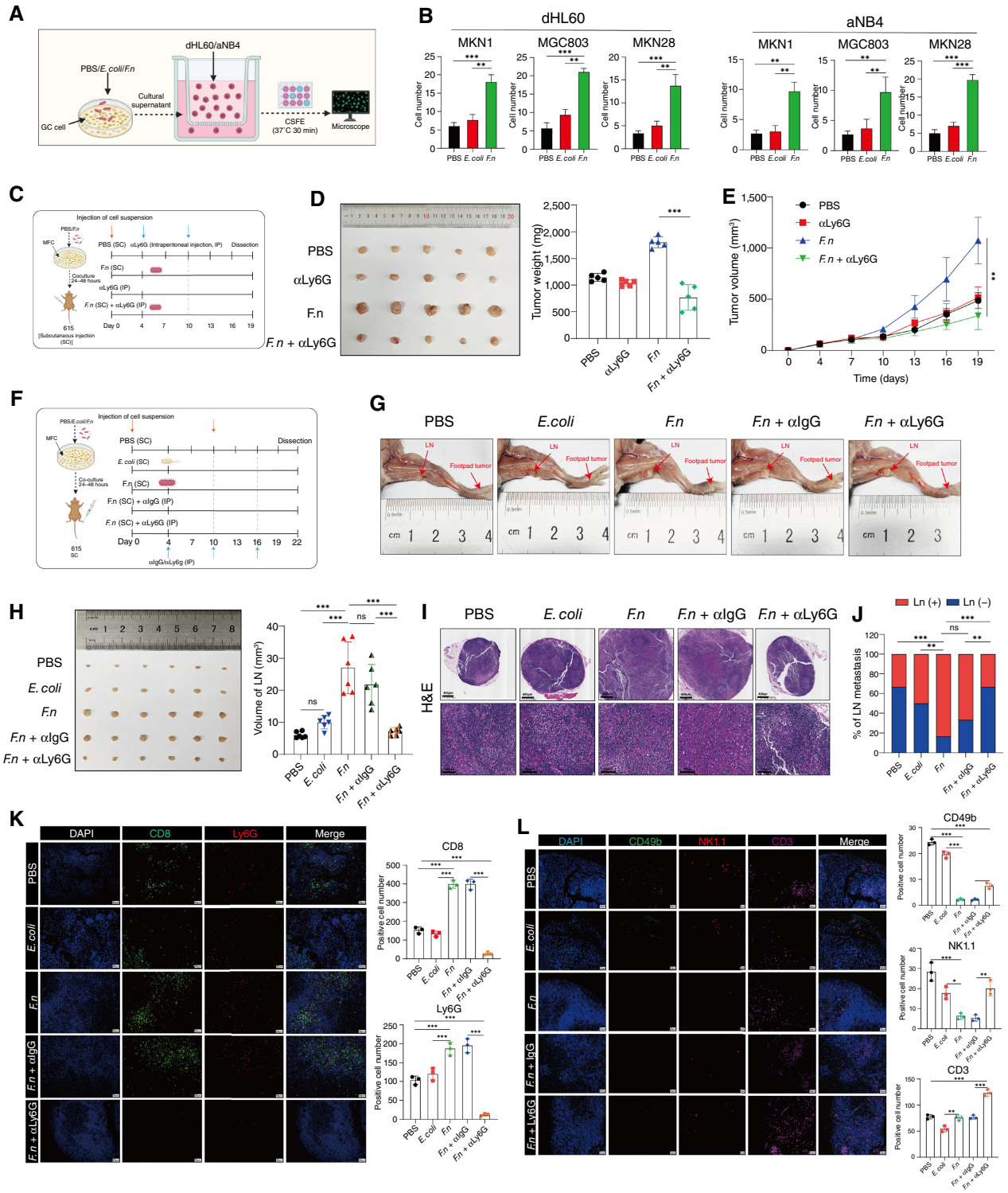

Figure 5.

F. nucleatum–mediated malignant progression of gastric cancer is significantly associated with neutrophil recruitment. **A,** Overview of neutrophils transwell experiment design. **B,** The transwell experiment and live cell fluorescence staining demonstrating the induction of dHL60 and aNB4 cell migration by the supernatant after *F. nucleatum* infects gastric cancer cells (the human acute promyelocyte HL60 and NB4 were induced to neutrophils). **C,** Pattern diagram showing the construction of the neutrophil depletion model. In this model, neutrophils were depleted using the anti-Ly6G antibody via intraperitoneal injection. Each group of mice consists of five individuals. **D,** General anatomy of subcutaneous tumors in different groups of (*Continued on the following page.*)

Fig. S2D–S2G). These data illustrate that *F. nucleatum* colonization occurred in the gastric mucosa and contributed to gastric cancer occurrence and development.

F. nucleatum facilitates malignant proliferation and metastasis of gastric cancer allografts *in vivo*

To explore the effect of *F. nucleatum* on gastric cancer cell proliferation, subcutaneous tumorigenesis models were constructed from immunodeficient BALB/c nude and immunocompetent 615 mice by subcutaneous implantation of MFC cells. Tumor growth in 615 mice infected with *F. nucleatum* was significantly faster than in the PBS and *E. coli* groups, with no differences observed between the PBS and *E. coli* groups. Ki67 expression was notably high in *F. nucleatum*–infected tumors. Intriguingly, *F. nucleatum*–infected gastric cancer cells demonstrated accelerated growth in immunocompetent mice compared with control groups but not in immunodeficient mice (**Fig. 2G–L**; Supplementary Fig. S2H and S2I). Meanwhile, footpad–popliteal LN metastasis and tail vein–lung metastasis models were constructed to examine *F. nucleatum*'s impact on gastric cancer cell metastasis *in vivo* (**Fig. 2M**). The tail vein–pulmonary metastasis model illustrated that *F. nucleatum* facilitated the distant metastasis of gastric cancer cells (**Fig. 2N**; Supplementary Fig. S2J). Similarly, the footpad–popliteal LN metastasis model replicates lymphatic metastasis in gastric cancer to some extent, enhancing the precision of *in vivo* evaluations. The *in vivo* imaging systems, LN volume, and H&E staining results revealed significantly increased popliteal LN metastasis in the *F. nucleatum*–infected group compared with control groups. Furthermore, survival curve analysis indicated that *F. nucleatum* infection in gastric cancer notably decreases survival time (**Fig. 2O–S**). Additionally, the CCK8 assay and cell monoclonal experiment suggested that *F. nucleatum* infection does not substantially alter gastric cancer cells' inherent malignant proliferation capacity (Supplementary Fig. S2K and S2L). Moreover, a tumor model was employed by orally gavaging *F. nucleatum* into immunocompetent mice, utilizing subcutaneous ectopic transplantation models in the axillary or inguinal regions. The findings demonstrated a considerably heightened malignant proliferative potential of tumors in the group that received oral gavage of *F. nucleatum*, exhibiting a notable increase in transplanted tumor volume compared with the control group (Supplementary Fig. S3A–S3E). These findings indicated that *F. nucleatum* might potentially alter the TIME, consequently influencing gastric cancer malignant progression.

F. nucleatum invades gastric cancer cells and establishes intracellular colonization

To explore how *F. nucleatum* affects gastric cancer cells, we cocultured *F. nucleatum* with gastric cancer cells and detected its localization within these cells. Scanning electron microscopy showed that *F. nucleatum* adhered to the gastric cancer cells' membrane surface (**Fig. 3A**). Further confocal fluorescence microscopy revealed *F. nucleatum* gathering around gastric cancer cells, with three-dimensional (3D) stereoscopic imaging revealing the same 3D plane between *F. nucleatum* and gastric cancer cells (**Fig. 3B**). Furthermore, upon infection with *F. nucleatum*, gastric cancer cells exhibited vesicular protrusions on their membranes (**Fig. 3C**). The findings indicated that *F. nucleatum* adhered to the membrane of gastric cancer cells and altered the membrane morphology. Transmission electron microscopy was employed to ascertain the presence of *F. nucleatum* in gastric cancer cells. Notably, *F. nucleatum* was found inside the cytoplasm, exhibiting clear structures with intact cell walls (**Fig. 3D**). When adhered to gastric cancer cell surfaces, *F. nucleatum* induced a finger-like structure around the cell membranes, similar to endocytosis (**Fig. 3E**).

To elucidate how *F. nucleatum* invades gastric cancer cells, fluorescent live cell imaging revealed the presence of numerous vesicle-like structures on the cell membrane surface, through which, *F. nucleatum* invaded the cells (**Fig. 3F**). Cell viability experiments showed that *F. nucleatum*–infected gastric cancer cells remained active (**Fig. 3G**). Antibiotic experiments revealed that *F. nucleatum* survives in the presence of cell-impermeable antibiotics (ampicillin and gentamicin) but not in the presence of cell-permeable antibiotics (doxycycline hydrochloride; **Fig. 3H**). Furthermore, treatment of gastric cancer cells with endocytosis inhibitors [ethylisopropylamiloride (EIPA), 50 μmol/L; genistein, 50 μmol/L; and chlorpromazine, 15 μmol/L] significantly decreased the presence of *F. nucleatum* in cells (**Fig. 3I**). To investigate whether intracellular *F. nucleatum* within gastric cancers affects the malignant progression of gastric cancer, we treated MFC cells with endocytosis inhibitors, followed by coculturing with *F. nucleatum*. After discarding the supernatant, the cell suspension was injected into the footpads of immunocompetent 615 mice. The results demonstrated that *F. nucleatum* promotes the malignant progression of gastric cancer, yet inhibiting endocytosis significantly reduced the tumor-promoting effect of *F. nucleatum*, suggesting that intracellular *F. nucleatum* mediates the malignant progression of gastric cancer (**Fig. 3J–L**). To elucidate the impact of intracellular *F. nucleatum* on the LN metastasis of gastric cancer cells, a mouse popliteal LN metastasis model was employed to track the activity trajectory of *F. nucleatum*. Intriguingly, FISH and transmission electron microscopy revealed *F. nucleatum* within the LNs (Supplementary Fig. S4A and S4B). Furthermore, bacterial culture confirmed that live *F. nucleatum* could translocate from the primary tumor to the LNs through intracellular colonization of gastric cancer cells (**Fig. 3M**). These results indicate that *F. nucleatum* invaded gastric cancer cells through endocytosis, establishing intracellular colonization and mediating gastric cancer malignant progression.

F. nucleatum–infected gastric cancer cells induce TAN recruitment and differentiation

To further explore the impact of *F. nucleatum* on the tumor microenvironment in gastric cancer, the subcutaneous tumorigenesis models of immunocompetent mice were constructed for scRNA-seq. Analysis revealed 17 subclusters and 8 major cell clusters (**Fig. 4A** and **B**; Supplementary Fig. S5A and S5B). To

(*Continued*.) 615 mice with Ly6G clearance. **E,** Growth curves displaying tumor volumes. **F,** The pattern diagram depicting the construction of the neutrophil depletion model in 615 mice. Each group of mice consists of six individuals. SC, subcutaneous injection. **G,** Anatomical illustration of the mouse footpad and popliteal LNs. **H,** The data pertaining to LN volume in the popliteal fossa demonstrating a notable reduction in the metastatic potential mediated by *F. nucleatum* following the depletion of neutrophils in mice. **I** and **J,** H&E staining revealing the distribution of tumor cells within different LN groups. **K** and **L,** MIF staining showing the expression level of CD8, Ly6G, CD49b, NK1.1, and CD3 in tumor tissues during neutrophil depletion following *F. nucleatum* infection. Data are presented as mean ± SEM. *, $P < 0.05$; **, $P < 0.01$; ***, $P < 0.001$; ns, not significant. Ln (−), LNs without metastasis; Ln (+), LNs with metastasis. **A**, **C**, and **F**, Created with BioRender.com. Zhang, T. (2025), https://BioRender.com/n44z466.

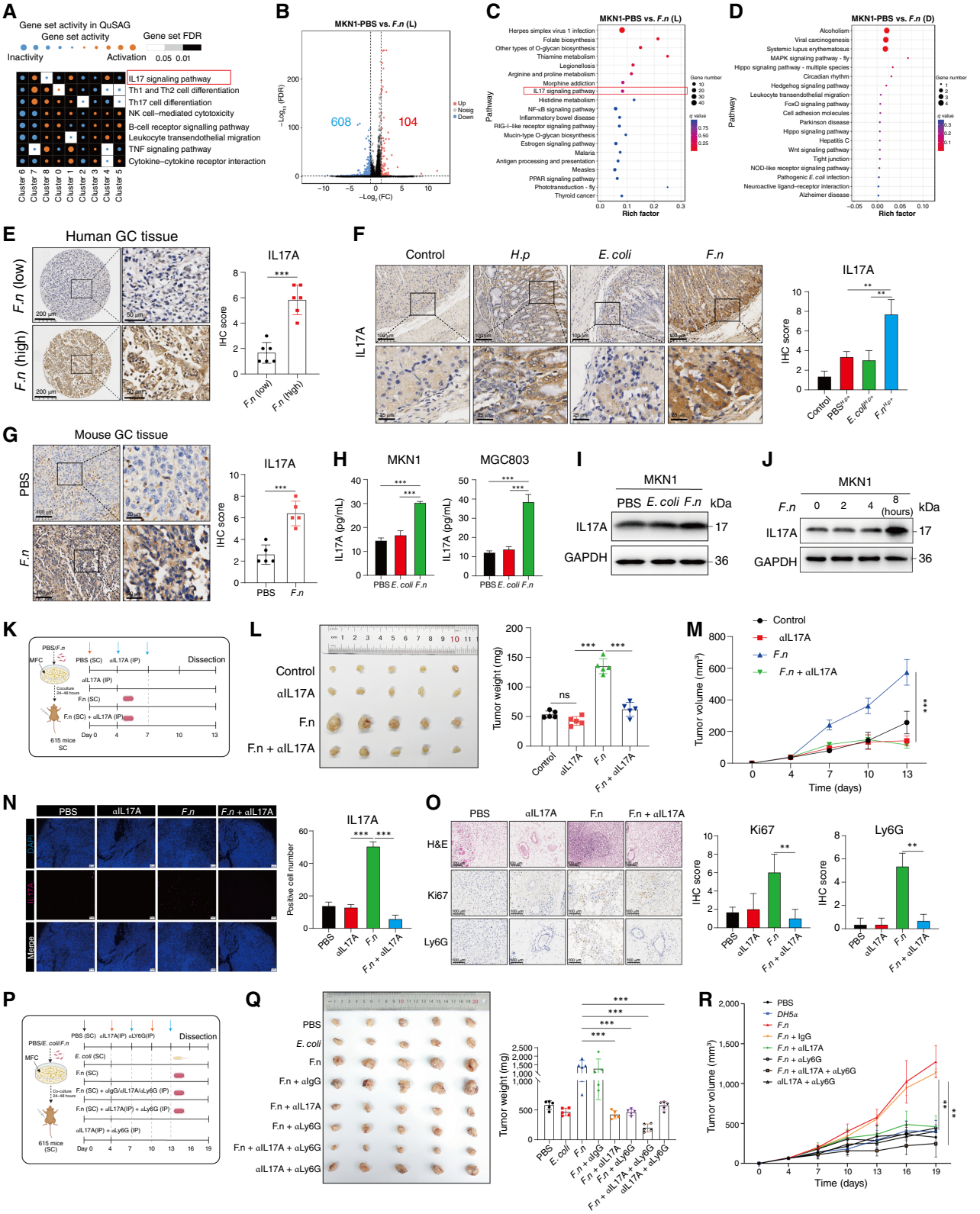
A
Gene set activity in QuSAG
Gene set activity
Gene set FDR
Inactivity
Activation
0.05 0.01
IL17 signaling pathway
Th1 and Th2 cell differentiation
Th17 cell differentiation
NK cell–mediated cytotoxicity
B-cell receptor signalling pathway
Leukocyte transendothelial migration
TNF signaling pathway
Cytokine–cytokine receptor interaction
Cluster 6
Cluster 7
Cluster 8
Cluster 0
Cluster 1
Cluster 2
Cluster 3
Cluster 4
Cluster 5
B
MKN1-PBS vs. F.n (L)
608
104
Up
Nosig
Down
C
MKN1-PBS vs. F.n (L)
Herpes simplex virus 1 infection
Folate biosynthesis
Other types of O-glycan biosynthesis
Thiamine metabolism
Legionellosis
Arginine and proline metabolism
Morphine addiction
IL17 signaling pathway
Histidine metabolism
NF-κB signaling pathway
Inflammatory bowel disease
RIG-I–like receptor signaling pathway
Mucin-type O-glycan biosynthesis
Estrogen signaling pathway
Malaria
Antigen processing and presentation
Measles
PPAR signaling pathway
Phototransduction - fly
Thyroid cancer
Pathway
Rich factor
Gene number
p.value
D
MKN1-PBS vs. F.n (D)
Alcoholism
Viral carcinogenesis
Systemic lupus erythematosus
MAPK signaling pathway - fly
Hippo signaling pathway - multiple species
Circadian rhythm
Hedgehog signaling pathway
Leukocyte transendothelial migration
FoxO signaling pathway
Cell adhesion molecules
Parkinson disease
Hippo signaling pathway
Hepatitis C
Wnt signaling pathway
Tight junction
NOD-like receptor signaling pathway
Pathogenic E.coli infection
Neuroactive ligand–receptor interaction
Alzheimer disease
Pathway
Rich factor
E
Human GC tissue
F.n (low)
F.n (high)
IL17A
IHC score
F.n (low)
F.n (high)
F
Control
H.p
E. coli
F.n
IL17A
IL17A
IHC score
Control
PBS
E. coli
F.n
G
Mouse GC tissue
PBS
F.n
IL17A
IHC score
PBS
F.n
H
MKN1
MGC803
IL17A (pg/mL)
PBS E. coli F.n
I
MKN1
PBS E. coli F.n
kDa
IL17A
GAPDH
17
36
J
MKN1
F.n
0 2 4 8 (hours)
kDa
IL17A
GAPDH
17
36
K
PBS/F.n
MFC
PBS (SC)
αIL17A (IP)
Dissection
αIL17A (IP)
Coculture 24–48 hours
F.n (SC)
F.n (SC) + αIL17A (IP)
615 mice SC
Day 0 4 7 10 13
L
Control
αIL17A
F.n
F.n + αIL17A
Tumor weight (mg)
ns
Control
αIL17A
F.n
F.n + αIL17A
M
Control
αIL17A
F.n
F.n + αIL17A
Tumor volume (mm³)
Time (days)
N
PBS
αIL17A
F.n
F.n + αIL17A
DAPI
IL17A
Merge
IL17A
Positive cell number
PBS
αIL17A
F.n
F.n + αIL17A
O
PBS
αIL17A
F.n
F.n + αIL17A
H&E
Ki67
Ly6G
Ki67
IHC score
Ly6G
IHC score
PBS
αIL17A
F.n
F.n + αIL17A
P
PBS/E. coli/F.n
MFC
PBS (SC) αIL17A(IP) αLY6G(IP)
Dissection
E. coli (SC)
F.n (SC)
Coculture 24–48 hours
F.n (SC) + αIgG/αIL17A/αLy6G (IP)
F.n (SC) + αIL17A(IP) + αLy6G (IP)
αIL17A(IP) + αLy6G (IP)
615 mice (SC)
Day 0 4 7 10 13 16 19
Q
PBS
E. coli
F.n
F.n + αIgG
F.n + αIL17A
F.n + αLy6G
F.n + αIL17A + αLy6G
αIL17A + αLy6G
Tumor weight (mg)
PBS
E. coli
F.n
F.n + αIgG
F.n + αIL17A
F.n + αLy6G
F.n + αIL17A + αLy6G
αIL17A + αLy6G
R
PBS
DH5α
F.n
F.n + IgG
F.n + αIL17A
F.n + αLy6G
F.n + αIL17A + αLy6G
αIL17A + αLy6G
Tumor volume (mm³)
Time (days)

observe the temporal heterogeneity of immune cell differentiation during gastric cancer progression, tumor tissues were collected from two periods (time 1 and time 2) and subjected to sequencing analysis. Time 1 corresponds to a 10-day tumor growth period, whereas time 2 represents a 19-day growth period, capturing the acute and chronic stages of tumor growth affected by *F. nucleatum*.

Remarkably, *F. nucleatum* group mice had more than three times the higher proportion of neutrophils in their subcutaneous tumors than in the control group. Furthermore, the proportion of neutrophils in late tumors increased distinctly after prolonged *F. nucleatum* infection. However, the population of other antitumor immune cells, such as B/plasma cells, decreased significantly (**Fig. 4C**; Supplementary Fig. S5C). Moreover, IHC, MIF, and flow cytometry results in tumor tissue of mice with *F. nucleatum* infection similarly confirmed this phenomenon (**Fig. 4D** and **E**). Additionally, the interaction network between neutrophils and other immune cells in tumor tissue was remarkably enhanced in the *F. nucleatum* infection group (**Fig. 4F**). These findings indicate that neutrophils are implicated in the malignant progression of gastric cancer.

Tumor immune responses are increasingly linked to neutrophils, often with poor clinical outcomes (22, 23). Correlation analysis of scRNA-seq revealed nine distinct TAN subclusters within tumor-infiltrating neutrophils, indicating their heterogeneity. Analysis of neutrophil proportions in different subgroups showed that those of Sell$^+$ neutrophils, Isg15$^+$ neutrophils, G5b and G5c staging neutrophils, and TAN-0 and TAN-3 were substantially declined. Conversely, those of Gbe$^+$ neutrophils, Wfdc21$^+$ neutrophils, G3 and G5a staging neutrophils, and TAN-1, TAN-2, TAN-4, TAN-5, TAN-6, and TAN-7 were considerably increased in tumors with *F. nucleatum* infection (**Fig. 4G**; Supplementary Fig. S5D–S5H). Combining the results of IHC and MIF, we found that intratumoral *F. nucleatum* infection reshaped the immune microenvironment of gastric cancer and exerted an inhibitory effect on antitumor immunity. Additionally, IHC results also showed significant recruitment of neutrophils in mouse tumor tissues and popliteal LNs after *F. nucleatum* infection, suggesting a crucial role of TANs in the malignant progression of gastric cancer (Supplementary Fig. S6A–S6D). These data indicate that *F. nucleatum*–infected gastric cancer cells induced neutrophil recruitment and promoted TANs to protumoral subtype differentiation.

To elucidate the impact of TANs on TIME in response to intratumoral *F. nucleatum* infection, we integrated a mouse model in which CD4$^+$ T cells, CD8$^+$ T cells, NK cells, and neutrophils were depleted. The results indicate that depletion of CD4$^+$ T cells and NK cells significantly increased tumor size in mice infected with *F. nucleatum*, whereas there was no significant change in tumor size when CD8$^+$ T cells were depleted. Expanding on our prior research discoveries, we hypothesize that within the tumor microenvironment infected with *F. nucleatum*, the antitumor efficacy facilitated by CD8$^+$ T cells is attenuated. Upon depleting neutrophils along with CD4$^+$ T cells, CD8$^+$ T cells, and NK cells simultaneously, we noted a notable decrease in the tumor's immunosuppressive effect following neutrophil clearance as opposed to scenarios in which neutrophils remained intact (Supplementary Figs. S7A–S7G and S8A–S8D). This confirms the critical role of neutrophils in reshaping the *F. nucleatum*–mediated immunosuppressive microenvironment.

Interestingly, we observed a significant upregulation of PD-L1 expression in TANs following *F. nucleatum* infection based on the single-cell sequencing gene set immune checkpoint expression analysis (**Fig. 4H** and **I**; Supplementary Fig. S9A). Upon clarification of the differentiation status of PD-L1$^+$ TANs in gastric cancer tissues with intratumoral *F. nucleatum* infection, a subsequent identification was conducted through flow cytometry analysis. The results demonstrated an elevated proportion of PD-L1$^+$ TANs within the *F. nucleatum*–infected mouse tumor tissue (**Fig. 4J**). Through Monocle2 (24) pseudotime analysis, it was determined that the *F. nucleatum* infection group primarily resided in the stage of tumor infiltration. Moreover, GO analysis and KEGG pathway enrichment analysis revealed that the *F. nucleatum*–infected group was associated with PD-L1 expression and the PD-1 checkpoint pathway in cancer, tumor angiogenesis, cell metastasis, immunosuppression, and inhibition of apoptosis (**Fig. 4K–N**). Furthermore, Western blotting results indicated that *in vitro* coculturing with *F. nucleatum* promoted elevated levels of PD-L1 expression in human neutrophils (Supplementary Fig. S9B and S9C). Additionally, IHC experiments demonstrated a positive correlation between the enrichment level of *F. nucleatum* and PD-L1 expression in both human and murine tissues (Supplementary Fig. S9D and S9E). These results suggested that intratumoral *F. nucleatum* infection promoted abnormal differentiation of PD-L1$^+$ TANs.

Figure 6.

F. nucleatum activates the IL17 signaling pathway within gastric cancer cells, mediating TAN recruitment and differentiation. **A,** The heatmap displaying the relative activation and significance of TAN-related immune pathways in different clusters. Orange, relative activation; blue, relative inactivity. The size of the bubble represents the relative level of activity or inactivity, with larger bubbles indicating a higher degree of alertness. **B,** The volcano map showing differential genes between the PBS group and the live *F. nucleatum*–infected group. *F.n*(L), live *F. nucleatum*. **C** and **D,** The visualization of a bubble plot representing the outcomes of KEGG enrichment analysis conducted on the genes associated with gastric cancer cells infected with live *F. n*(L) and *F. n*(D). *F.n*(D), heat-inactivated *F. nucleatum*. **E,** Representative IHC images of IL17A expression in human gastric cancer tissues with high and low abundance of *F. nucleatum*. **F,** Representative IHC images of IL17A expression in gastric mucosa of mice infected by *F. nucleatum*. The specimen used in this figure is derived from mouse gastric mucosal tissue, as shown in **Fig. 2C**. **G,** IHC staining showing the expression level of IL17A protein in gastric cancer tissues of mice after *F. nucleatum* infection. **H,** The ELISA analysis revealed the secretion level of IL17 by gastric cancer cells following infection with *F. nucleatum*. **I,** The Western blot results demonstrating the expression of IL17 protein in gastric cancer cells subsequent to infection with *F. nucleatum* and across varying MOI values. **J,** Western blot analysis indicates the expression levels of IL17A protein in gastric cancer cells following *F. nucleatum* infection at different time intervals. **K,** The pattern diagram showing the construction of the IL17 clearance model in mice. Each group of mice consists of five individuals. **L,** General anatomy of subcutaneous tumors in different groups of 615 mice with IL17 clearance. **M,** Growth curves displaying tumor volumes. **N,** Immunofluorescence results showing the expression of IL17A in tumor tissues with IL17A clearance. **O,** IHC staining demonstrating significantly weakened expression of Ki67 and Ly6G when IL17A was cleared in the tumor tissue with *F. nucleatum* infection. **P,** The pattern diagram demonstrating the construction of the IL17 and Ly6G clearance model. Each group of mice consists of five individuals. **Q,** General anatomy of subcutaneous tumors in different groups of 615 mice with IL17 and Ly6G clearance. **R,** Growth curves displaying tumor volumes. Data are presented as mean ± SEM. *, $P < 0.05$; **, $P < 0.01$; ***, $P < 0.001$. **K** and **P**, Created with BioRender.com. Zhang, T. (2025), https://BioRender.com/b17e915.

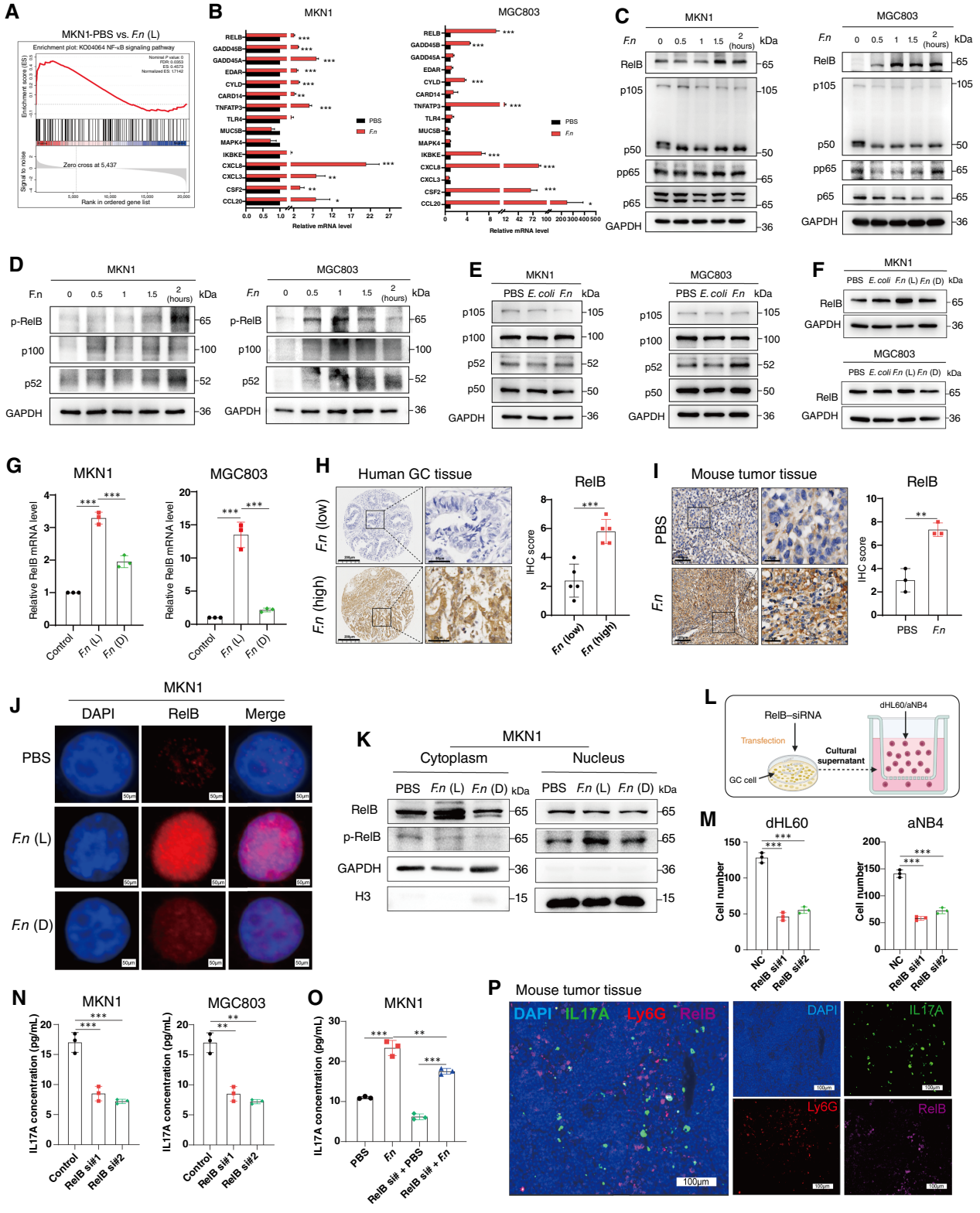

Figure 7.

F. nucleatum activates the IL17 signaling pathway through RelB–IL17A interaction. **A,** The gene set enrichment analysis revealed a significant upregulation of the NF-κB signaling pathway in association with live *F. nucleatum* infection. **B,** qRT-PCR results showing RNA expression of differentially expressed genes in the IL17 signaling pathways after *F. nucleatum* infection with gastric cancer cells. **C** and **D,** Western blot results showing the levels (*Continued on the following page.*)

F. nucleatum–mediated malignant progression of gastric cancer is significantly associated with neutrophil recruitment

To validate the effect of *F. nucleatum* on gastric cancer cells and neutrophils, the "*F. nucleatum*–gastric cancer cells–neutrophils" coculture model was constructed. The supernatant from the coculture of *F. nucleatum* with gastric cancer cells was centrifuged and placed in the outer chamber, and then induced differentiation of neutrophils dHL60 and aNB4 was added to the inner chamber. Notably, the *F. nucleatum* group had higher neutrophil migrations than the control group (**Fig. 5A** and **B**; Supplementary Fig. S9F), indicating that supernatant from the *F. nucleatum*–infected gastric cancer cells induced neutrophil recruitment.

A neutrophil depletion model was constructed in immunocompetent mice to investigate the relationship between *F. nucleatum*–mediated gastric cancer malignant progression and neutrophil recruitment. The tumor and LN volume, tumor weight, H&E staining, and LN metastasis rate results revealed that the impact of *F. nucleatum* on tumor proliferation and metastasis substantially diminished upon removal of neutrophils (**Fig. 5C–J**; Supplementary Fig. S9G). These data indicate that neutrophil recruitment plays a crucial role in the process by which *F. nucleatum* promotes gastric cancer malignant progression. MIF unexpectedly revealed a substantial increase in $CD8^+$T cells in regions enriched with TANs in *F. nucleatum*–infected mice. Following neutrophil depletion, there was a notable decrease in the $CD8^+$ T-cell proportion, indicating that the suppressed tumor immune response influenced by *F. nucleatum* correlated with the recruitment of neutrophils (**Fig. 5K** and **L**). To clarify whether intracellular *F. nucleatum* affects neutrophil recruitment, we also constructed a coculture model involving doxycycline and endocytosis inhibitors. Interestingly, these results revealed a notable decrease in the number of recruited neutrophils when doxycycline and endocytosis inhibitors were used, suggesting further that intracellular *F. nucleatum* promotes neutrophil recruitment mediated by tumor cells (Supplementary Fig. S10A–S10D).

F. nucleatum activates the IL17 signaling pathway within gastric cancer cells and mediates TAN recruitment and differentiation

To explore the molecular mechanism of *F. nucleatum*–infected gastric cancer cell–mediated TAN recruitment, further scRNA-seq analysis was performed to identify downstream signaling pathways. GO and KEGG enrichment analysis indicated that the promotion of neutrophil activation by *F. nucleatum* infection was enriched in the IL17 signaling pathway (Supplementary Fig. S11A and S11B). Subsequent gene set activity analysis demonstrated higher scores in protumoral TANs in the IL17 signaling pathway (**Fig. 6A**). Furthermore, IL17RA (the receptor of IL17) expression was correlated with neutrophil polarization and development, showing higher expression in the *F. nucleatum* group than in the control group (Supplementary Fig. S11C). Pseudotime analysis revealed that high expression of IL17RA prolonged the lifespan of TANs and promoted the differentiation of the neutrophil-promoting tumor subtype (Supplementary Fig. S11D). These findings indicated a strong correlation between the activation of the IL17 pathway and neutrophil recruitment in gastric cancer.

To examine the molecular mechanisms of *F. nucleatum* infection in gastric cancer cells, we cocultured MKN1 cells with live (L) or heat-inactivated (D) *F. nucleatum* and obtained RNA for transcriptome sequencing. Gene expression comparison revealed distinct patterns in the PBS group versus the *F.n*(L) group (712 genes), the PBS group versus the *F.n*(D) group (14 genes), and the *F.n*(L) group versus the *F.n*(D) group (805 genes; Supplementary Tables S10–S12). Compared with the *F.n*(D) group, both KEGG pathway enrichment analysis and gene set enrichment analysis revealed significant activation of the IL17 signaling pathway in the *F.n*(L) group (**Fig. 6B–D**; Supplementary Fig. S11E–S11H). Combined scRNA-seq of tumor tissues and cellular transcriptome sequencing revealed that *F. nucleatum* activated the IL17 pathway within gastric cancer cells, thereby promoting neutrophil recruitment. Analysis of TCGA data indicated that IL17A was highly expressed in human gastric cancer tissues and was associated with poor prognosis (Supplementary Fig. S11I and S11J). IHC staining revealed increased expression of IL17A in human and mouse gastric cancer tissue enriched with *F. nucleatum*. Furthermore, IHC staining demonstrated significantly enhanced expression of IL17A in the gastric mucosa of the primary gastric cancer model with the *F.n* group. Higher expression of IL17A was significantly associated with an adverse prognosis in gastric cancer (**Fig. 6E–G**). ELISA and Western blot analysis also demonstrated significantly increased IL17A protein levels in *F. nucleatum*–infected gastric cancer cells (**Fig. 6H–J**). Moreover, in the *F. nucleatum* infection group, cytokines related to the IL17 pathway were secreted more frequently, and neutrophil recruitment of cytokines, such as IL1β, IL8, and G-CSF, was significantly enhanced *in vitro* (Supplementary Fig. S11K). Additionally, the endocytosis inhibitor and permeabilizing antibiotics (doxycycline) markedly decreased the secretion of IL17A by gastric cancer cells. Compared with the group without endocytosis inhibitors and doxycycline, we observed a significant decrease in the level of IL17A in the cell culture supernatant when endocytosis inhibitors and doxycycline were added during the coculture of *F. nucleatum* and gastric cancers (Supplementary Fig. S12A–S12D). This indicates that intratumoral *F. nucleatum* infection promoted the expression and secretion of IL17A within tumor cells.

To further elucidate how *F. nucleatum* influences the expression of PD-L1 in TANs, we initially performed a correlation analysis utilizing the TCGA database. Our examination of the TCGA database revealed a positive association between the levels of IL17A and PD-L1 expression within human gastric cancer tissues. Furthermore, *in vitro*

(*Continued*.) of NF-κB pathway-related proteins increased after *F. nucleatum* infection with gastric cancer cells, among which, p52 and RelB were more prominent. **E,** Western blot was used to compare the changes in the levels of p52 and p50 proteins. **F,** Western blot results demonstrating the expression level of RelB in gastric cancer cells infected with live *F. nucleatum* (denoted as "L") or upon deactivation of *F. nucleatum* (denoted as "D"). **G,** The qRT-PCR results showing the expression level of RelB within gastric cancer cells infected with *F. nucleatum*. **H,** IHC staining revealed the expression level of RelB in human gastric cancer tissue enriched with *F. nucleatum*. **I,** IHC staining results displaying the expression of RelB in gastric cancer tissues of mice after *F. nucleatum* infection. **J,** Immunofluorescence. showing the status of RelB–nuclear translocation in gastric cancer cells after *F. nucleatum* infection. **K,** Western blot results depicting the status of RelB–nuclear translocation in gastric cancer cells after *F. nucleatum* infection. **L,** Overview of the neutrophil transwell experiment design. GC, gastric cancer. **M,** The transwell experiment results demonstrating the chemotactic ability of dHL60 and aNB4 cells after knocking down RelB in gastric cancer cells. NC, negative control. **N,** ELISA results displaying the level of IL17A secretion after knocking down gastric cancer cells and neutrophil RelB genes. **O,** ELISA results showed the secretion level of IL17A in gastric cancer cells caused by *F. nucleatum* infection after RelB knockdown. **P,** Immunofluorescence. results showing the expression and positioning of IL17A, Ly6G, and RelB in tumor tissues. Data are presented as mean ± SEM. *, $P < 0.05$; **, $P < 0.01$; ***, $P < 0.001$. **L**, Created with BioRender.com. Zhang, T. (2025), https://BioRender.com/g61x838.

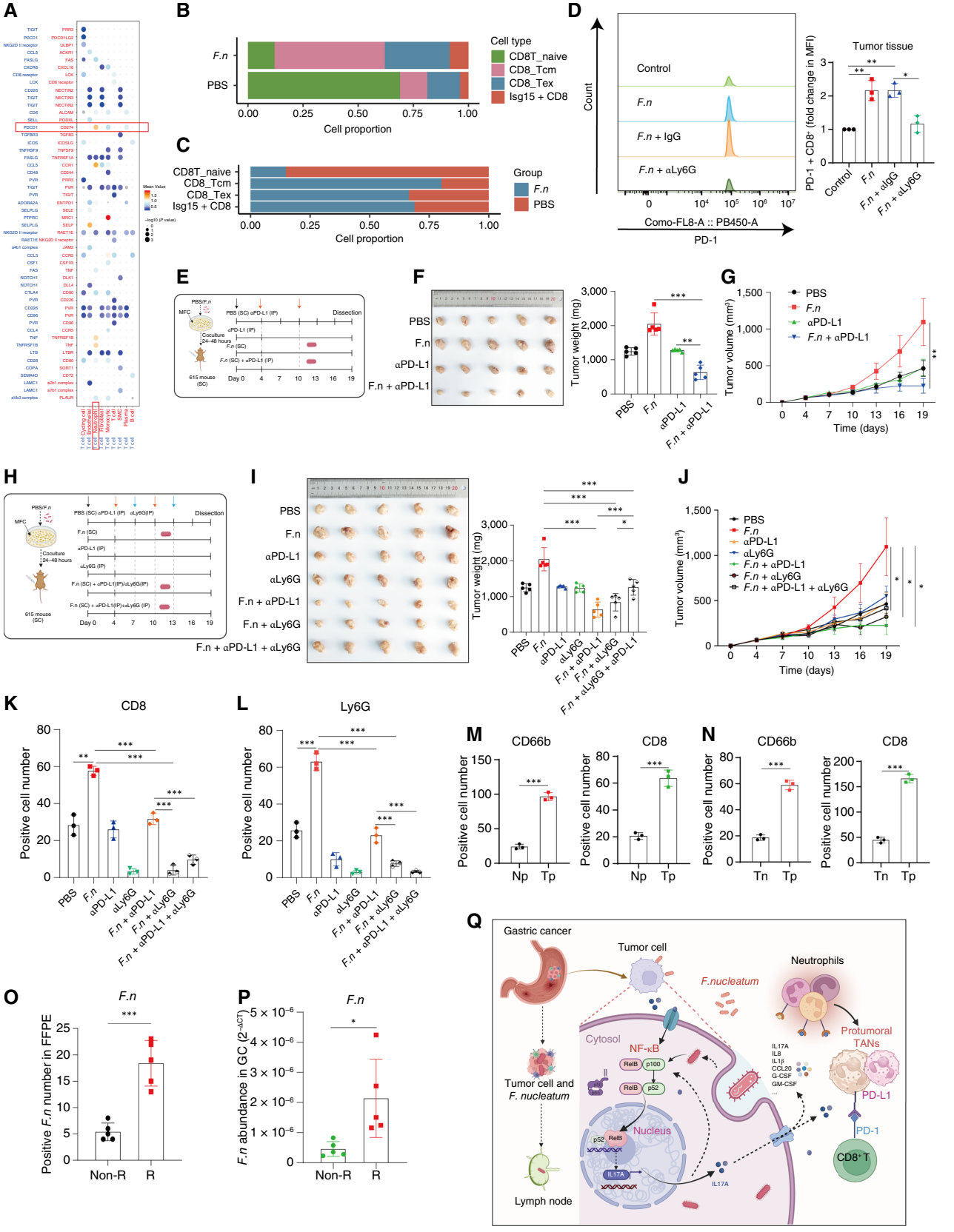
A
B
Cell type
CD8T_naive
CD8_Tcm
CD8_Tex
Isg15 + CD8
F.n
PBS
Cell proportion
C
Group
F.n
PBS
D
Control
F.n
F.n + IgG
F.n + αLy6G
Count
Como-FL8-A :: PB450-A
PD-1
Tumor tissue
PD-1 + CD8+ (fold change in MFI)
E
Dissection
Day 0
F
Tumor weight (mg)
G
Tumor volume (mm³)
Time (days)
H
I
J
K
CD8
Positive cell number
L
Ly6G
M
CD66b
Np
Tp
N
Tn
O
Positive F.n number in FFPE
Non-R
R
P
F.n abundance in GC (2^-ΔCT)
Q
Gastric cancer
Tumor cell
F.nucleatum
Neutrophils
Protumoral TANs
Cytosol
NF-κB
Nucleus
PD-L1
PD-1
CD8+ T
Tumor cell and F. nucleatum
Lymph node

cell culture experiments with the addition of IL17A demonstrated a significant upregulation of PD-L1 expression in humanized neutrophils (Supplementary Fig. S12E and S12F). Subsequent flow cytometry analysis revealed a significant decrease in the proportion of PD-L1^{+}Ly6G^{+} cells in tumor tissues from *F. nucleatum*–infected mice following treatment with IL17A neutralizing antibodies (Supplementary Fig. S12G). Recent studies have shown that the innate immune system plays a crucial role in initiating immune responses. Specifically, activation of the cyclic GMP-AMP synthase (cGAS)–stimulator of interferon genes (STING) pathway can generate type I interferon, inducing both innate and adaptive immune responses, thus playing an essential role in tumor immunotherapy (25–30). Our findings demonstrated that the enhanced expression of PD-L1 on neutrophils induced by *F. nucleatum* was suppressed upon treatment with the cGAS–STING pathway inhibitor (RU.521). Furthermore, the upregulation of neutrophil PD-L1 expression triggered by IL17A could be reversed by the cGAS–STING pathway inhibitor (RU.521; Supplementary Fig. S12H and S12I). These findings suggest that *F. nucleatum* might influence the aberrant expression of PD-L1 in TANs through the cGAS–STING pathway regulated by IL17A.

An anti–IL17A treatment model was constructed to validate the function of IL17A in TAN recruitment in gastric cancer. Notably, treatment with anti–IL17A remarkably reduced the volume of subcutaneous tumors in the *F. nucleatum*–infected group. IHC staining further indicated a notable decrease in the expression of Ki67 and Ly6G following anti–IL17A treatment (**Fig. 6K–O**). To elucidate the roles of IL17A and neutrophils in *F. nucleatum*–mediated tumor promotion, we developed a combined model involving neutrophil depletion and anti–IL17A treatment. Remarkably, both anti–IL17 treatment and neutrophil depletion separately blocked *F. nucleatum*–mediated tumor progression. Furthermore, treatment using anti–IL17A combined with neutrophil depletion was more effective in *F. nucleatum*–infected mice compared with noninfected mice. Conversely, the combined anti–IL17A treatment and neutrophil depletion showed no significant difference in mice without *F. nucleatum* infection (**Fig. 6P–R**). These outcomes illuminate the potential of anti–IL17A treatment in inhibiting *F. nucleatum*–mediated tumor progression, emphasizing the heightened effectiveness of anti–IL17A treatment in combination with neutrophil depletion, specifically within *F. nucleatum*–enriched gastric cancer.

F. nucleatum activates the IL17 signaling pathway through RelB–IL17A interaction

NF-κB is a pivotal regulator of genes responsible for encoding inflammatory mediators. Recent studies have revealed that *F. nucleatum* upregulates the canonical NF-κB pathway, augmenting the expression of proinflammatory cytokines, thereby triggering colonic inflammation and carcinogenesis (31, 32). The gene set enrichment analysis revealed that NF-κB signaling pathways were enriched in *F. nucleatum*–infected gastric cancer cells (**Fig. 7A**), suggesting the involvement of the NF-κB pathway in neutrophil activation and the malignant progression of gastric cancer. In this study, NF-κB and IL17 signaling pathways were thought to be closely linked in tumor cell–neutrophil interactions.

To determine the interaction between the NF-κB pathway and the IL17 pathway, we conducted transcriptomic differential gene analysis coupled with qRT-PCR assays. There was a considerable upregulation of RelB, TNFATP3, CXCL3, CXCL8, CSF2, and CCL20 genes in both the NF-κB pathway and the IL17 pathway (**Fig. 7B**; Supplementary Fig. S13A). RelB was widely recognized as a key protein in the noncanonical NF-κB pathway. The Western blot analysis revealed a remarkable increase in p52 and RelB protein levels among NF-κB subunits in gastric cancer cells (**Fig. 7C–E**). Remarkably, qRT-PCR and Western blot results indicate substantial upregulation of RelB in the *F.n*(L) group but no significant change in the *F.n*(D) group. IHC staining demonstrated heightened expression of RelB in human and mouse gastric cancer tissue rich in *F. nucleatum*. Additionally, RelB was highly expressed in gastric cancer tissues and correlated with poor prognosis of gastric cancer according to the TCGA cohort. Analysis of immune cell infiltration in the TCGA database indicated a positive correlation between RelB expression and neutrophil infiltration in gastric cancer (**Fig. 7F–I**; Supplementary Fig. S13B–S13F). Furthermore, *F. nucleatum* infection promoted the phosphorylation and nuclear translocation of RelB proteins (**Fig. 7J** and **K**; Supplementary Fig. S13G–S13I).Additionally, the transwell experiment results demonstrated a significant reduction in the chemotactic ability of neutrophils after knocking down RelB in gastric cancer cells (**Fig. 7L** and **M**). These results indicated that RelB might be an essential target gene of the NF-κB/IL17 signaling pathway.

Upon further RelB knockdown in gastric cancer cells, secretion levels of IL17A proteins were substantially decreased and significantly inhibited following *F. nucleatum* infection (**Fig. 7N** and **O**). When IL17A was added to the culture medium, RelB protein levels were significantly increased. Immunofluorescence colocalization experiments revealed a significant upregulation of RelB, IL17A, and the neutrophil-associated protein Ly6G in mice infected with *F. nucleatum* tumor tissues. Moreover, these proteins exhibited a spatially correlated distribution (**Fig. 7P**; Supplementary Fig. S13J and S13K). Our data indicated that the cross-talk interaction between activation of RelB in NF-κB and IL17 pathways significantly enhances IL17A secretion and further induces neutrophil recruitment and differentiation.

Figure 8.

F. nucleatum mediates TAN recruitment to promote gastric cancer immune evasion and boost PD-L1 blockade efficacy. **A,** CellPhoneDB analysis of scRNA-seq displaying the interaction relationship of proteins between designated receptor cell taxa. **B,** Bar plot showing a comparison of the proportions of the main cell types in different samples. **C,** A comparison of the proportions of the main cell types between PBS1, PBS2, *F.n*1, and *F.n*2 was displayed by the bar plot. **D,** Flow cytometry analysis revealed the expression levels of PD-1 on CD8^{+} T cells in tumor tissues of the mouse neutrophil depletion model. **E,** The pattern diagram depicting the construction of the PD-L1 clearance model in mice. Each group of mice consists of five individuals. **F,** General anatomy of subcutaneous tumors in different groups of 615 mice with PD-L1 clearance. **G,** Growth curves display tumor volumes. **H,** The pattern diagram depicting the construction of the IL17A and Ly6G clearance model in mice. Each group of mice consists of five individuals. SC, subcutaneous injection. **I,** General anatomy of subcutaneous tumors in different groups of 615 mice with IL17A and Ly6G clearance. **J,** Growth curves display tumor volumes. **K** and **L,** MIF staining revealed the proportion of CD8^{+} T cells and Ly6G^{+} neutrophils in *F. nucleatum*–infected tumor tissue with PD-L1 clearance. **M** and **N**, MIF staining revealed the proportion of CD66b^{+} neutrophils in gastric cancer tissue with high *F. nucleatum* density. Np, paranormal tissue of gastric cancer with lymph node metastasis; Tn, tumor tissues without lymph node metastasis; Tp, tumor tissues with lymph node metastasis. **O,** *In situ* hybridization revealed the abundance of *F. nucleatum* in gastric cancer tissues of patients responding to anti–PD-L1 therapy. FFPE, formalin-fixed, paraffin-embedded. **P,** The qRT-PCR analysis indicated the abundance of *F. nucleatum* in the primary tumors of patients with gastric cancer (GC) exhibiting a response to PD-L1 therapy. **Q**, Mechanism diagram of the whole article. Data are presented as mean ± SEM. *, $P < 0.05$; **, $P < 0.01$; ***, $P < 0.001$. **E**, **H**, and **Q**, Created with BioRender.com. Zhang, T. (2025), https://BioRender.com/o74e010 (**E** and **H**) and https://BioRender.com/h16l685 (**Q**).

F. nucleatum mediates TAN recruitment to promote gastric cancer immune evasion and boost PD-L1 blockade efficacy

In **Fig. 5K** and **L**, we observed a significant enrichment of $CD8^+$T cells in the area recruited by neutrophils in tumor tissues following *F. nucleatum* infection. Furthermore, after depleting neutrophils, $CD4^+$ T cells, $CD8^+$ T cells, and NK cells, we observed a significant reduction in the tumor's immunosuppressive influence following neutrophil clearance compared with situations in which neutrophils were preserved. This finding underscores the pivotal role of neutrophils in modifying the *F. nucleatum*–mediated immunosuppressive microenvironment.

To identify the interaction between neutrophils and other immune cells, we applied CellPhoneDB analysis (19). Upon *F. nucleatum* infection, there was a noticeable enhancement in the interaction between PD-$L1^+$ TANs and PD-1^+ T cells (**Fig. 8A**). A substantial upregulation of PD-1 expression in tumor tissue was noted following *F. nucleatum* infection (Supplementary Fig. S14A). Examination of different $CD8^+$ T-cell types showed a significant increase in exhausted $CD8^+$ T ($CD8^+$ Tex) cells after *F. nucleatum* infection, suggesting the recruitment and differentiation of TANs further contribute to $CD8^+$ T-cell exhaustion (**Fig. 8B** and **C**; Supplementary Fig. S14B). Moreover, flow cytometry and Western blotting analysis revealed a significant upregulation of PD-L1 expression in human neutrophils and TANs from mice upon infection with *F. nucleatum* (**Fig. 8D**). Based on pseudotime analysis, $CD8^+$ T cells differentiate in the direction of PD-1^{high} in response to *F. nucleatum* infection, and gene set immune checkpoint expression analysis and KEGG analysis revealed significant enrichment of the PD-L1 pathway in $CD8^+$ T cells of the *F. nucleatum* group (Supplementary Fig. S14C–S14J). Subsequent analysis using flow cytometry unveiled a notable increase in the percentage of PD-1^+ $CD8^+$ T cells in tumor tissues following *F. nucleatum* infection. Conversely, upon neutrophil depletion, the proportion of PD-1^+ $CD8^+$ T cells conspicuously decreased, suggesting a close association between the recruitment of neutrophils and $CD8^+$ T cells as well as their exhaustion within the tumor microenvironment (**Fig. 8D**; Supplementary Fig. S15A and S15B). Moreover, as described in **Fig. 7**, after simultaneous neutrophil elimination, the tumor volume in mice noticeably decreased compared with when solely clearing $CD8^+$ T cells, indicating a partial reduction in $CD8^+$ T-cell exhaustion upon neutrophil clearance, consequently unleashing the antitumor activity of $CD8^+$ T cells. These results indicate that *F. nucleatum* contributes to $CD8^+$ T-cell exhaustion by enhancing the expression of PD-L1 in TANs.

Subsequently, an anti–PD-L1 treatment model in mice was established to evaluate the efficacy of PD-L1 immunotherapy in gastric cancer with *F. nucleatum* infection. Tumor volume considerably decreased in the *F. nucleatum* group, indicating a superior response to anti–PD-L1 treatment compared with the control group (**Fig. 8E–G**). By creating a mouse model with neutrophil depletion and anti–PD-L1 treatment, we found that the impact of the anti–PD-L1 treatment lessened when neutrophils were depleted (**Fig. 8H–J**). This confirmed a strong correlation between anti–PD-L1 treatment in *F. nucleatum*–infected mice and neutrophil recruitment. Further, MIF staining revealed a significant decrease in the proportion of $CD8^+$ T cells and TANs in *F. nucleatum*–infected tumor tissue with anti–PD-L1 treatment (**Fig. 8K** and **L**; Supplementary Fig. S15C). Meanwhile, immunofluorescence staining indicated a notable increase in $CD66b^+$ neutrophils in gastric cancer tissue with high *F. nucleatum* density. Correspondingly, areas rich in CD66b showed an increase in $CD8^+$ T cells (**Fig. 8M** and **N**; Supplementary Fig. S15D and S15E). In situ hybridization and qRT-PCR results revealed a high abundance of *F. nucleatum* in gastric cancer tissues of patients responding to anti–PD-L1 treatment (**Fig. 8O** and **P**; Supplementary Fig. S15F). PET-CT showed a significant reduction in metastatic lesions in patients with gastric cancer with high *F. nucleatum* levels following anti–PD-L1 immunotherapy (Supplementary Fig. S15G).

Discussion

In recent years, an increasing number of studies have revealed a close relationship between microbiota and the malignant progression of tumors, particularly within the gut microbiota (33, 34). Current research gradually confirms that intratumoral bacteria play crucial roles in the malignant progression and treatment outcomes of tumors (35). Recently, although extensive research has focused on the association between *F. nucleatum* and malignant progression in cancers, notably colorectal cancer, there has been a notable scarcity of investigations about the interplay of *F. nucleatum* with the TIME. Previous research has predominantly focused on the microbiota's impact on tumor cells directly (36–38). Nonetheless, the advancement of tumors toward malignancy typically entails the modulation of the microenvironment (39). Furthermore, recent studies emphasize the intratumoral microbiota's significant role in promoting immune escape and influencing immunotherapy efficacy in cancer (40–44). Our research elucidates that intracellular *F. nucleatum* promotes the recruitment and differentiation of TANs, reshaping the immunosuppressive microenvironment and leading to $CD8^+$ T-cell exhaustion. Mechanistically, *F. nucleatum* invades gastric cancer cells and activates the IL17/NF-κB/RelB signaling pathway, thereby promoting the recruitment of TANs and their differentiation into a protumoral subtype, which further reshapes the TIME. Moreover, intratumoral *F. nucleatum* contributes to the exhaustion of $CD8^+$ T cells by inducing high expression of PD-L1 in TANs, subsequently facilitating immune evasion in gastric cancer and augmenting the effectiveness of PD-L1 immune therapy. This study elucidated a novel mechanism by which intratumoral microbiota influences immune escape in gastric cancer and mediates the response to immunotherapy, thereby providing new theoretical foundations for the treatment of patients with gastric cancer.

The precise involvement of intracellular microbiota in gastric cancer malignant progression and immune microenvironment remodeling remains largely ambiguous. Prior studies indicate an inverse correlation between *F. nucleatum* presence in colorectal cancer tissues and the abundance of tumor-infiltrating lymphocytes, affecting antitumor immune response suppression (45, 46). Fu and colleagues (47) confirmed that intracellular bacteria carried by circulating breast cancer cells enhance fluid shear resistance by reorganizing the actin cytoskeleton during tumor cell metastasis and colonization. Our findings indicated that intratumoral *F. nucleatum* colonization occurred in gastric cancer cells and contributed to gastric cancer malignant progression. Furthermore, scRNA-seq showed that *F. nucleatum*–infected gastric cancer cells significantly enhanced neutrophil recruitment in the tumor microenvironment. Neutrophils have dual roles in immune responses. Research into their biological activities related to antitumor and tumor-promoting functions has gained increased attention (7). Neutrophil recruitment is primarily initiated by inflammatory mediators such as histamine, cysteine leukotrienes, and cytokines at the endothelial surface when sentinel leukocytes encounter pathogens in tissues (48–50). Jaillon and colleagues and Scapini and colleagues (51, 52) found that neutrophils are a marker of acute inflammation associated with activated, localized, and regulated immune responses. Moreover, neutrophils can suppress

T-cell proliferation and hamper their activity (53). In our study, TANs in *F. nucleatum*–infected tumor tissues mainly tended toward protumoral subtype differentiation. Intratumoral *F. nucleatum* induced neutrophil-mediated $CD8^+$ T-cell exhaustion to further promote gastric cancer immune evasion. Our findings support that *F. nucleatum* promotes gastric cancer development by altering the TIME through neutrophil recruitment.

Neutrophils promote cancer development both directly and indirectly (54). For instance, TANs remain alive while releasing neutrophil extracellular traps, which promotes the proliferation of cancer cells (55). Kong and colleagues (56) discovered that *F. nucleatum* induces the formation of neutrophil extracellular traps by activating the Toll-like receptor 4–reactive oxygen species pathway and the NOD1/NOD2 signaling pathways in neutrophils, thereby facilitating the progression of colorectal cancer. Similarly, neutrophils induce the transition from gastric mucosal epithelial cells to mesenchymal cells, promoting the migration and invasion of gastric cancer cells (57). Our results identified a close relationship between IL17 signaling and TAN recruitment, and the data showed that intracellular *F. nucleatum* activated the NF-κB pathway to enhance IL17A secretion within gastric cancer cells. Moreover, there is cross-talk between NF-κB and IL17 signaling pathways, further promoting neutrophil recruitment through a cascade amplification mechanism. Our data indicated a novel mechanism by which *F. nucleatum* promotes IL17A–mediated neutrophil recruitment and protumoral TAN differentiation to promote gastric cancer malignant progression. Remarkably, aberrant PD-L1 expression has been noted in these protumoral TANs, suggesting a potential link between *F. nucleatum*–mediated neutrophil recruitment and PD-L1 therapy.

Anti–PD-1/anti–PD-L1 treatment is progressively reshaping the overarching treatment strategy for patients with gastric cancers (58, 59). However, gastric cancer represents a highly heterogeneous malignant tumor, wherein most tumor tissues demonstrate an immunosuppressive state, significantly affecting the effectiveness of immune checkpoint inhibitor therapy (60–62). Recent research has revealed that the influence of microbiota on tumor immunotherapy is multifaceted. Jiang and colleagues (41) discovered that a high abundance of *F. nucleatum* limits the infiltration and effector function of $CD8^+$ T cells within the tumor through its metabolite succinate, thereby promoting resistance to anti–PD-1 monoclonal antibody therapy. Conversely, Gao and colleagues (42) demonstrated that *F. nucleatum* may heighten tumor sensitivity to PD-L1 blockade therapy by activating the STING signaling pathway. Our scRNA-seq data revealed a significant interaction between PD-1 in the $CD8^+$ T-cell subpopulation and PD-L1 in protumoral TANs. Furthermore, the *F. nucleatum*–infected gastric cancer showed a more favorable response to anti–PD-L1 treatment *in vivo*, attributed to the recruitment of $PD\text{-}L1^+$ TANs. Our findings demonstrate that anti–PD-1/PD-L1 treatment can be enhanced by *F. nucleatum* infection, which mainly contributes to TAN recruitment and differentiation. Therefore, this provides a theoretical basis and treatment strategy for the clinical application of anti–PD-1/anti–PD-L1 immunotherapy in patients with gastric cancer.

Overall, *F. nucleatum* mediates neutrophil recruitment to alter the TIME in gastric cancer. Mechanistically, intratumoral *F. nucleatum* invading gastric cancer cells activates NF-κB/IL17 signaling, promoting TAN recruitment and protumoral TAN differentiation in TIME. This process exhausts $CD8^+$ T cells, promotes immune evasion, and enhances the effectiveness of anti–PD-1/anti–PD-L1 immunotherapy in gastric cancer. These findings reveal novel mechanisms through which *F. nucleatum* affects gastric cancer malignant progression, providing new insights for developing effective treatment strategies.

Authors' Disclosures

T. Zhang reports grants from the Guangdong Provincial Natural Science Foundation, the Guangdong Provincial Health Commission, and the Fundamental Research Funds for the Central Universities, Sun Yat-sen University during the conduct of the study. Y. Qian reports grants from the Guangzhou Science and Technology Programme and the Guangdong Provincial Natural Science Foundation project during the conduct of the study. J. Chen reports grants from the Guangdong Provincial Natural Science Foundation project and the National Natural Science Foundation of China during the conduct of the study. S. Cai reports grants from the National Natural Science Foundation of China and the Guangdong Provincial Natural Science Foundation during the conduct of the study. No disclosures were reported by the other authors.

Authors' Contributions

T. Zhang: Conceptualization, data curation, funding acquisition, validation, methodology, writing–original draft. **Y. Li:** Conceptualization, data curation, funding acquisition, writing–original draft. **E. Zhai:** Conceptualization, data curation, methodology, writing–original draft. **R. Zhao:** Software, formal analysis, funding acquisition, writing–review and editing. **Y. Qian:** Data curation, software, formal analysis, funding acquisition, writing–review and editing. **Z. Huang:** Validation, methodology. **Y. Liu:** Validation, methodology. **Z. Zhao:** Validation, methodology. **X. Xu:** Software, visualization. **J. Liu:** Visualization, methodology. **Z. Li:** Formal analysis, methodology. **Z. Liang:** Formal analysis, visualization. **R. Wei:** Software, formal analysis. **L. Ye:** Formal analysis, visualization. **J. Ma:** Formal analysis, visualization. **Q. Wu:** Conceptualization, resources, funding acquisition, project administration, writing–review and editing. **J. Chen:** Conceptualization, resources, supervision, funding acquisition, writing–review and editing. **S. Cai:** Conceptualization, resources, supervision, funding acquisition, project administration, writing–review and editing.

Acknowledgments

This study was supported by the National Natural Science Foundation of China grant 82173239 (S. Cai), 82472904 (J. Chen), and 82100626 (R. Zhao); Guangdong Provincial Natural Science Foundation project grant 2023A1515111152 (T. Zhang), 2021A1515110759 (Y. Qian), 2023A1515011187 (Y. Qian), 2022A1515011534 (S. Cai), and 2024A1515010739 (J. Chen); Key-Area Research and Development Program of Guangdong Province grant 2022B1111070006 (Q. Wu); GDAS' Project of Science and Technology Development 2022GDASZH-2022010101 (Q. Wu); Guangdong Provincial Health Commission grant A2024052 (T. Zhang); The Fundamental Research Funds for the Central Universities, Sun Yat-sen University 24qnpy329 (T. Zhang); and Guangzhou Nansha Technology Plan Project (2024MS006, 2023MS003; J. Ma). This study was also supported by the Guangdong Province Excellent Youth Team Project (2024B1515040029), led by Professor Junchao Cai at Sun Yat-sen University. Additionally, we extend our thanks to Novel Bio for their support in single-cell sequencing.

Note

Supplementary data for this article are available at Cancer Research Online (http://cancerres.aacrjournals.org/).

Received July 23, 2024; revised December 7, 2024; accepted February 19, 2025; posted first February 24, 2025.

References

1. Sung H, Ferlay J, Siegel RL, Laversanne M, Soerjomataram I, Jemal A, et al. Global cancer statistics 2020: GLOBOCAN estimates of incidence and mortality worldwide for 36 cancers in 185 countries. CA Cancer J Clin 2021; 71:209–49.

2. Peek RM Jr, Blaser MJ. Helicobacter pylori and gastrointestinal tract adenocarcinomas. Nat Rev Cancer 2002;2:28–37.
3. Marshall BJ, Warren JR. Unidentified curved bacilli in the stomach of patients with gastritis and peptic ulceration. Lancet 1984;1:1311–5.
4. Lofgren JL, Whary MT, Ge Z, Muthupalani S, Taylor NS, Mobley M, et al. Lack of commensal flora in Helicobacter pylori-infected INS-GAS mice reduces gastritis and delays intraepithelial neoplasia. Gastroenterology 2011;140:210–20.
5. Fu K, Cheung AHK, Wong CC, Liu W, Zhou Y, Wang F, et al. Streptococcus anginosus promotes gastric inflammation, atrophy, and tumorigenesis in mice. Cell 2024;187:882–96.e17.
6. Que H, Fu Q, Lan T, Tian X, Wei X. Tumor-associated neutrophils and neutrophil-targeted cancer therapies. Biochim Biophys Acta Rev Cancer 2022;1877:188762.
7. Jaillon S, Ponzetta A, Di Mitri D, Santoni A, Bonecchi R, Mantovani A. Neutrophil diversity and plasticity in tumour progression and therapy. Nat Rev Cancer 2020;20:485–503.
8. Wigerblad G, Kaplan MJ. Neutrophil extracellular traps in systemic autoimmune and autoinflammatory diseases. Nat Rev Immunol 2023;23:274–88.
9. Xiong S, Dong L, Cheng L. Neutrophils in cancer carcinogenesis and metastasis. J Hematol Oncol 2021;14:173.
10. Faget J, Peters S, Quantin X, Meylan E, Bonnefoy N. Neutrophils in the era of immune checkpoint blockade. J Immunother Cancer 2021;9:e002242.
11. Rubinstein MR, Wang X, Liu W, Hao Y, Cai G, Han YW. Fusobacterium nucleatum promotes colorectal carcinogenesis by modulating E-cadherin/β-catenin signaling via its FadA adhesin. Cell Host Microbe 2013;14:195–206.
12. Kostic AD, Chun E, Robertson L, Glickman JN, Gallini CA, Michaud M, et al. Fusobacterium nucleatum potentiates intestinal tumorigenesis and modulates the tumor-immune microenvironment. Cell Host Microbe 2013;14:207–15.
13. Gur C, Ibrahim Y, Isaacson B, Yamin R, Abed J, Gamliel M, et al. Binding of the Fap2 protein of Fusobacterium nucleatum to human inhibitory receptor TIGIT protects tumors from immune cell attack. Immunity 2015;42:344–55.
14. Yu T, Guo F, Yu Y, Sun T, Ma D, Han J, et al. Fusobacterium nucleatum promotes chemoresistance to colorectal cancer by modulating autophagy. Cell 2017;170:548–63.e16.
15. Yamamura K, Izumi D, Kandimalla R, Sonohara F, Baba Y, Yoshida N, et al. Intratumoral Fusobacterium nucleatum levels predict therapeutic response to neoadjuvant chemotherapy in esophageal squamous cell carcinoma. Clin Cancer Res 2019;25:6170–9.
16. Kostic AD, Gevers D, Pedamallu CS, Michaud M, Duke F, Earl AM, et al. Genomic analysis identifies association of Fusobacterium with colorectal carcinoma. Genome Res 2012;22:292–8.
17. Yu T, Guo F, Yu Y, Sun T, Ma D, Han J, et al. Fusobacterium nucleatum promotes chemoresistance to colorectal cancer by modulating autophagy. Cell 2017;170:548–63.e16.
18. Percie du Sert N, Hurst V, Ahluwalia A, Alam S, Avey MT, Baker M, et al. The ARRIVE guidelines 2.0: updated guidelines for reporting animal research. Br J Pharmacol 2020;177:3617–24.
19. Efremova M, Vento-Tormo M, Teichmann SA, Vento-Tormo R. CellPhoneDB: inferring cell-cell communication from combined expression of multi-subunit ligand-receptor complexes. Nat Protoc 2020;15:1484–506.
20. Chen T, Chen X, Zhang S, Zhu J, Tang B, Wang A, et al. The Genome Sequence Archive family: toward explosive data growth and diverse data types. Genomics Proteomics Bioinformatics 2021;19:578–83.
21. CNCB-NGDC Members and Partners. Database Resources of the National Genomics Data Center, China National Center for Bioinformation in 2022. Nucleic Acids Res 2022;50:D27–D38.
22. Ng MSF, Kwok I, Tan L, Shi C, Cerezo-Wallis D, Tan Y, et al. Deterministic reprogramming of neutrophils within tumors. Science 2024;383:eadf6493.
23. Shaul ME, Fridlender ZG. Tumour-associated neutrophils in patients with cancer. Nat Rev Clin Oncol 2019;16:601–20.
24. Trapnell C, Cacchiarelli D, Grimsby J, Pokharel P, Li S, Morse M, et al. The dynamics and regulators of cell fate decisions are revealed by pseudotemporal ordering of single cells. Nat Biotechnol 2014;32:381–6.
25. Lee J-J, Kim SY, Kim SH, Choi S, Lee B, Shin J-S. STING mediates nuclear PD-L1 targeting-induced senescence in cancer cells. Cell Death Dis 2022;13:791.
26. Jiang M, Chen P, Wang L, Li W, Chen B, Liu Y, et al. cGAS-STING, an important pathway in cancer immunotherapy. J Hematol Oncol 2020;13:81.
27. Loo TM, Miyata K, Tanaka Y, Takahashi A. Cellular senescence and senescence-associated secretory phenotype via the cGAS-STING signaling pathway in cancer. Cancer Sci 2020;111:304–11.
28. Yang H, Wang H, Ren J, Chen Q, Chen ZJ. cGAS is essential for cellular senescence. Proc Natl Acad Sci U S A 2017;114:E4612–20.
29. Dixon CR, Malik P, de Las Heras JI, Saiz-Ros N, de Lima Alves F, Tingey M, et al. STING nuclear partners contribute to innate immune signaling responses. iScience 2021;24:103055.
30. Guo Q, Chen X, Chen J, Zheng G, Xie C, Wu H, et al. STING promotes senescence, apoptosis, and extracellular matrix degradation in osteoarthritis via the NF-κB signaling pathway. Cell Death Dis 2021;12:13.
31. Chen Y, Chen Y, Cao P, Su W, Zhan N, Dong W. Fusobacterium nucleatum facilitates ulcerative colitis through activating IL-17F signaling to NF-κB via the upregulation of CARD3 expression. J Pathol 2020;250:170–82.
32. Yang Y, Weng W, Peng J, Hong L, Yang L, Toiyama Y, et al. Fusobacterium nucleatum increases proliferation of colorectal cancer cells and tumor development in mice by activating toll-like receptor 4 signaling to nuclear factor-κb, and up-regulating expression of microRNA-21. Gastroenterology 2017;152:851–66.e24.
33. Carmody RN, Sarkar A, Reese AT. Gut microbiota through an evolutionary lens. Science 2021;372:462–3.
34. Ternes D, Tsenkova M, Pozdeev VI, Meyers M, Koncina E, Atatri S, et al. The gut microbial metabolite formate exacerbates colorectal cancer progression. Nat Metab 2022;4:458–75.
35. Zepeda-Rivera M, Minot SS, Bouzek H, Wu H, Blanco-Míguez A, Manghi P, et al. A distinct Fusobacterium nucleatum clade dominates the colorectal cancer niche. Nature 2024;628:424–32.
36. Holt RA, Cochrane K. Tumor potentiating mechanisms of Fusobacterium nucleatum, A multifaceted microbe. Gastroenterology 2017;152:694–6.
37. Parhi L, Alon-Maimon T, Sol A, Nejman D, Shhadeh A, Fainsod-Levi T, et al. Breast cancer colonization by Fusobacterium nucleatum accelerates tumor growth and metastatic progression. Nat Commun 2020;11:3259.
38. Hara Y, Baba Y, Oda E, Harada K, Yamashita K, Toihata T, et al. Presence of Fusobacterium nucleatum in relation to patient survival and an acidic environment in oesophagogastric junction and gastric cancers. Br J Cancer 2024;131:797–807.
39. Galeano Niño JL, Wu H, LaCourse KD, Kempchinsky AG, Baryiames A, Barber B, et al. Effect of the intratumoral microbiota on spatial and cellular heterogeneity in cancer. Nature 2022;611:810–17.
40. Davar D, Dzutsev AK, McCulloch JA, Rodrigues RR, Chauvin J-M, Morrison RM, et al. Fecal microbiota transplant overcomes resistance to anti-PD-1 therapy in melanoma patients. Science 2021;371:595–602.
41. Jiang S-S, Xie Y-L, Xiao X-Y, Kang Z-R, Lin X-L, Zhang L, et al. Fusobacterium nucleatum-derived succinic acid induces tumor resistance to immunotherapy in colorectal cancer. Cell Host Microbe 2023;31:781–97.e9.
42. Gao Y, Bi D, Xie R, Li M, Guo J, Liu H, et al. Fusobacterium nucleatum enhances the efficacy of PD-L1 blockade in colorectal cancer. Signal Transduct Target Ther 2021;6:398.
43. Cao Y, Xia H, Tan X, Shi C, Ma Y, Meng D, et al. Intratumoural microbiota: a new frontier in cancer development and therapy. Signal Transduct Target Ther 2024;9:15.
44. Fu A, Yao B, Dong T, Cai S. Emerging roles of intratumor microbiota in cancer metastasis. Trends Cell Biol 2023;33:583–93.
45. Mima K, Sukawa Y, Nishihara R, Qian ZR, Yamauchi M, Inamura K, et al. Fusobacterium nucleatum and T cells in colorectal carcinoma. JAMA Oncol 2015;1:653–61.
46. Hamada T, Zhang X, Mima K, Bullman S, Sukawa Y, Nowak JA, et al. Fusobacterium nucleatum in colorectal cancer relates to immune response differentially by tumor microsatellite instability status. Cancer Immunol Res 2018;6:1327–36.
47. Fu A, Yao B, Dong T, Chen Y, Yao J, Liu Y, et al. Tumor-resident intracellular microbiota promotes metastatic colonization in breast cancer. Cell 2022;185:1356–72.e26.
48. Phillipson M, Kubes P. The neutrophil in vascular inflammation. Nat Med 2011;17:1381–90.
49. Ley K, Laudanna C, Cybulsky MI, Nourshargh S. Getting to the site of inflammation: the leukocyte adhesion cascade updated. Nat Rev Immunol 2007;7:678–89.
50. Brinkmann V, Reichard U, Goosmann C, Fauler B, Uhlemann Y, Weiss DS, et al. Neutrophil extracellular traps kill bacteria. Science 2004;303:1532–5.

51. Jaillon S, Galdiero MR, Del Prete D, Cassatella MA, Garlanda C, Mantovani A. Neutrophils in innate and adaptive immunity. Semin Immunopathol 2013;35:377–94.
52. Scapini P, Cassatella MA. Social networking of human neutrophils within the immune system. Blood 2014;124:710–9.
53. Galli SJ, Borregaard N, Wynn TA. Phenotypic and functional plasticity of cells of innate immunity: macrophages, mast cells and neutrophils. Nat Immunol 2011;12:1035–44.
54. Giese MA, Hind LE, Huttenlocher A. Neutrophil plasticity in the tumor microenvironment. Blood 2019;133:2159–67.
55. Cristinziano L, Modestino L, Loffredo S, Varricchi G, Braile M, Ferrara AL, et al. Anaplastic thyroid cancer cells induce the release of mitochondrial extracellular DNA traps by viable neutrophils. J Immunol 2020;204:1362–72.
56. Kong X, Zhang Y, Xiang L, You Y, Duan Y, Zhao Y, et al. Fusobacterium nucleatum-triggered neutrophil extracellular traps facilitate colorectal carcinoma progression. J Exp Clin Cancer Res 2023;42:236.
57. Wu L, Saxena S, Singh RK. Neutrophils in the tumor microenvironment. Adv Exp Med Biol 2020;1224:1–20.
58. Shi T, Zhang Y, Wang Y, Song X, Wang H, Zhou X, et al. DKK1 promotes tumor immune evasion and impedes anti-PD-1 treatment by inducing immunosuppressive macrophages in gastric cancer. Cancer Immunol Res 2022;10:1506–24.
59. Wang Z-X, Pan Y-Q, Li X, Tsubata T, Xu R-H. Immunotherapy in gastrointestinal cancers: advances, challenges, and countermeasures. Sci Bull (Beijing) 2023;68:763–6.
60. Alsina M, Arrazubi V, Diez M, Tabernero J. Current developments in gastric cancer: from molecular profiling to treatment strategy. Nat Rev Gastroenterol Hepatol 2023;20:155–70.
61. Guan W-L, He Y, Xu R-H. Gastric cancer treatment: recent progress and future perspectives. J Hematol Oncol 2023;16:57.
62. Mager LF, Burkhard R, Pett N, Cooke NCA, Brown K, Ramay H, et al. Microbiome-derived inosine modulates response to checkpoint inhibitor immunotherapy. Science 2020;369:1481–9.